Aerosol transport in idealized wind-wave systems

Espen Åkervik

FFI Norwegian Defence Research Establishment

Aerosol transport in idealized wind-wave systems

Espen Åkervik

Summary

This report deals with aerosol transport in turbulent wind over water waves. For simple terrain onshore, there appears to be consensus that aerosol transport is well described by simple models. However, for complex terrain or geometry, such as urban environments, advanced computational fluid dynamics models are needed. Although the wind flow over water is reminiscent of the wind over flat terrain onshore, there are some important differences, such as altered heat fluxes and the presence of wind generated waves.

In this report we explore three idealized flow regimes that may be encountered offshore. In the first one, the wind is not capable of creating waves. The result is a flat surface. The second regime is when the winds are sufficiently strong to generate water waves. These so-called wind waves are slow compared to the local wind, and their bulk effect is to provide aerodynamic drag. The third regime occurs when distantly generated waves propagate into regions of calmer winds. These so called swell waves have fast propagation speeds compared to the local wind.

We compare aerosol transport for these three cases by means of computational fluid dynamics (CFD) on a laboratory scale. In order to capture the effect of deposition on the water surface, we solved the turbulent motion in the air as well as the wave propagation in the water, and a particle method is used to track a large number of aerosols of different sizes.

In line with existing literature, we find that the wind sea behaves as a rough surface. For the dispersion of aerosols, this has two major consequences. Firstly, cross-stream transport is enhanced. This leads to a wider plume for all particle sizes studied. Secondly, and arguably most important, there is a downward transport mechanism present, which leads to deposition of larger aerosols at the surface. Consequently, for wind seas there is reduced air concentrations of larger sized aerosols compared to the flat surface case.

The plume width and the plume arrival time of the swell regime and the flat surface regime are almost indiscernible. However, since swell waves feed momentum to the air, there is an upward transport mechanism, which is most effective for larger aerosols. The most important consequence of this is that the plume is transported downstream almost as an isolated blob, thus counteracting the near surface clustering present in the flat surface case. This leads to higher concentrations downstream of the source.

For small aerosols, the plume shape and arrival time is fairly similar for the three regimes. This suggests that simple operational dispersion models, such as Gaussian models, may be used for transport of neutral gases over waves. However, the results point to some differences in the concentration distribution between the three cases.

For larger aerosols, this report shows clear evidence of altered dynamics both for wind seas and swell seas compared to the flat boundary layer flow. These effects are currently not captured by simple dispersion models but may prove to be important.

The current results are obtained at a laboratory scale, and further research is warranted to investigate the effects on relevant atmospheric scales.

Sammendrag

Denne rapporten tar for seg aerosoltransport ved turbulent vind over vannbølger. For enkelt terreng over land ser det ut til å være enighet om at aerosoltransport er godt beskrevet av forenklede modeller. Vi vet likevel at terreng eller geometri kan være kompleks, som i urbane miljøer. Da er det nødvendig med avanserte beregningsmodeller. Den turbulente strømningen over vann er til forveksling lik strømningen over flatt terreng på land, men det er noen viktige forskjeller. For det første endres varmetransporten sammenlignet med forhold på land. For det andre genereres bølger som et resultat av vinden.

I denne rapporten utforsker vi tre idealiserte strømningsregimer som kan oppstå ved strømning over vann. I det første er vinden for svak til å generere bølger. Dermed forblir havoverflaten flat. Det andre regimet er når vinden er sterk nok til å generere vannbølger. Disse såkalte vindbølgene er langsomme sammenlignet med den lokale vinden. Hovedeffekten er å bidra med aerodynamisk motstand for vinden. Det tredje regimet oppstår når bølger som har blitt generert et annet sted forplanter seg inn i områder med roligere vind. Disse kalles dønninger, og har rask forplantningshastighet sammenlignet med den lokale vinden.

I tråd med eksisterende litteratur finner vi at vindbølger oppfører seg som en ru overflate. For spredning av aerosoler har dette to vesentlige følger. For det første forsterkes de turbulente spenningene, noe som fører til en bredere spredningssky. Det andre og kanskje viktigste er at bølgene bidrar med en nedoverrettet transportmekanisme. Denne fører til avsetning av større partikler på overflaten. Resultatet er lavere luftkonsentrasjoner av aerosoler sammenliknet med en flat overflate.

I dønningsregimet er bredden på spredningen og ankomsttiden til aerosolskyen til forveksling lik det som oppstår ved en flat overflate. Imidlertid er dønninger karakterisert av en oppoverrettet transportmekanisme, der bølgene gir energi til vinden. Den viktigste konsekvensen av dette er at bølgebevegelsen ser ut til å dytte aerosoler vekk fra overflaten. Denne dyttingen motvirker at aerosoler klynger seg nær overflaten, slik tilfellet er for en flat overflate. Aerosolskyen transporteres derfor i dette tilfellet mer som en konsentrert sky sammenlignet med den flate overflaten. Dette kan føre til lokale regioner med høyere konsentrasjoner.

For små aerosoler er både formen på og ankomsttiden til spredningsskyen relativt lik for de tre regimene. Dette antyder at forenklede spredningsmodeller, som de såkalte Gauss-modellene, kan være egnet til å beskrive turbulent transport av nøytrale gasser over bølger. Imidlertid er det noen forskjeller i konsentrasjoner for de tre regimene.

For større aerosoler viser denne rapporten klare bevis på endret spredningsdynamikk. Dette gjelder både for vindsjøregimet og for dønningsregimet sammenlignet med spredning over en flat overflate. Disse effektene er ikke fanget av dagens forenklede spredningsmodeller.

Resultatene i denne rapporten er oppnådd på en såkalt laboratorieskala. Det er en skala som er mye mindre enn den faktiske skalaen til vind-bølge interaksjon i atmosfæren. Det virker nødvendig å undersøke om disse effektene fortsatt er tilstede på atmosfærisk skala.

Contents

1   Introduction

Release and aerial dispersion of contaminants may threaten the lives and health of the population and adversely affect the environment. To identify effective countermeasures, responsible authorities benefits from having reliable estimates of the spatial and temporal evolution of the averaged and instantaneous concentration levels of a contaminant cloud.

For onshore conditions, it is more or less accepted that in the absence of tall buildings and terrain variation, simplified models, such as the so called Gaussian plume models, provide sufficiently reliable predictions of the transport (Hanna *et al.*, 1982). However, in environments where buildings are present and/or where terrain variation is substantial, complex flow patterns emerge. These flow patterns can only be properly described by advanced computational models, such as computational fluid dynamics models (CFD) for buildings and fine scale terrain and numerical weather predictions models for large scale terrain. Such computations are computational costly, but recent advances in post-processing methods has rendered it possible to utilise their results in real time prediction software (Boris *et al.*, 2004).

For offshore conditions, it is reasonable to expect that the Gaussian plume framework will serve as a good tool for aerosol transport prediction. This is justified by the observation that the sea surface can be seen as a very smooth surface compared to most onshore surfaces. The effectiveness of simplified models rely on the validity of simple descriptions of the flow field. Indeed, for atmospheric boundary layers it has proven useful to model the mean wind profile as a simple log profile (Stull, 1988)

$$U(z) = (u_*/\kappa) \log(z/z_0), \tag{1.1}$$

where u_* is the friction velocity (typically on the order of $U_{10m}/u_* \approx 20$), $\kappa \approx 0.4$ is the von-Karman constant, z is the distance above ground, and z_0 is the so called roughness length.

Over land the roughness length is clearly defined based on the surface types such as sand, snow, grass, forest, etc. (Arya, 1975). Moreover, turbulence levels are consistent with surface roughness, which implies that a rough surface has higher turbulence intensity than a smooth surface and therefore leads to more effective mixing. However, over sea, the surface roughness is not a simple function of the wave shape. Charnock (1955) proposed, based on dimensional arguments, that the roughness due to waves should be given as

$$z_0 = \alpha_c u_*^2/g, \tag{1.2}$$

where α_c is the Charnocks parameter, u_* is the friction velocity, and g is the gravitational acceleration. The Charnocks parameter depends in a complicated manner on the wave speed, wind speed and the wave height (Deskos *et al.*, 2021). Two possible parametrization strategies to deal with this problem in coupled atmospheric models can be found in Janssen *et al.* (2002); Fairall *et al.* (2003). The development of these parametrizations has been greatly aided by several large scale measurement campaigns (Hasselmann *et al.*, 1973; Fairall *et al.*, 2003; Belamari, 2005; Edson *et al.*, 2007). However, since measurements at the moving surface has been a difficult task, there are still major uncertainties as to the underlying mechanisms of transport between air and sea.

Therefore, during the last 20 years the research community has pursued the idea of performing resolved simulations of wind/wave systems Mastenbroek *et al.* (1996); Sullivan *et al.* (2000); Yang & Shen (2010); Åkervik & Vartdal (2019). However, due to the immense computational effort required, most work has been restricted to small scales and a fixed/idealised wave propagating underneath the air. Nevertheless, this effort has led to better understanding of the interaction mechanism at the surface. Detailed studies of scalar transport are scarce, but Yang & Shen (2017)

studied scalar transport in the air phase subject to propagating waves. The authors used a constant scalar value at the surface (reminiscent of sea surface temperature), and found scaling properties similar to the standard boundary layer in terms of the roughness. When it comes to aerosol transport across the interface we have found very few attempts at fine scale studies. Exceptions include Mortazavi *et al.* (2016); Deike *et al.* (2016), where in both cases air entrainment to the water phase was studied by means of resolved two-phase simulations.

Waves arise as the response to the wind forcing at the surface. The underlying mechanism that governs this process is not fully understood. Operational wave forecasting relies on the celebrated critical layer mechanism of Miles (1957). However, Belcher & Hunt (1993, 1998) argued that the Miles mechanism could only be active for relatively fast waves. They reintroduced an updated version of the Jeffreys (1925) sheltering mechanism for slow waves. Waves that propagate faster than the bulk wind typically emerge as the result of nonlinear interaction of slower waves, or as the result of distantly storm-generated waves that enter domains of lighter winds. The momentum flux between the air and the sea is dramatically altered in the presence of these fast moving waves (Sullivan *et al.*, 2008; Kahma *et al.*, 2016). Examples of simplified models for the air-side response in this regime include Cohen & Belcher (1999); Kudryavtsev *et al.* (2001); Åkervik & Vartdal (2019).

The enhancement/reversal of momentum flux for flow over waves is bound to have an influence on the transport characteristic of aerosols, both in the air phase and across the interface. On a short time scale there is mass transfer across the interface, which includes dry and wet deposition and re-aerosolization by means of wave breaking Donelan (1998); Deike *et al.* (2016). This is a complicated process that depends on the chemical properties of the aerosols. Even if one ignores these relatively small scale effects, the large scale transfer of momentum and energy - associated with the growth and decay of waves - will have a direct mechanical effect on transport of aerosols both in the air phase and across the interface. This is the focus of the present report.

In the report, we solve the coupled two-phase Navier–Stokes equations, similar to Mortazavi *et al.* (2016), to study the influence of waves on aerosol transport. In particular, the aerosol transport for flat surface, wind sea and swell sea is compared. Contrary to Deike *et al.* (2016) we do not consider breaking waves. Instead, we seek to isolate the transport mechanism present for simple propagating waves. We employ a particle method (Lagrangian) for the aerosol transport with background velocity fields obtained by a continuum method (Eularian), as opposed to Yang & Shen (2017), who use a continuum method (Eularian) for both. The advantage of the current choice of method, is that finite size particles (aerosols) can be considered, thus enabling deposition at the interface. As most other detailed studies to date, we are limited to study the flow under very idealized conditions. In particular, we are far from studying the problem at real scales. Nevertheless it is hoped that the insight and some of the conclusions offered at a model scale can be employed in more realistic settings. Additionally, we restrict ourselves to the study of simple propagating waves, although this is not required by the methodology. However, given the complexity of the flow, we consider it of vital interest to simplify the system as much as possible in order to be able to extract usable knowledge.

2 Problem definition

2.1 Two-phase fluid motion

The motion of fluids can be described by a set of conservation equations along with a number of constitutive relations describing the material properties of the fluid. We here consider incompressible, immiscible, Newtonian fluids for which the motion is governed by conservation of mass and momentum (Kundu *et al.*, 2012)

$$\nabla \cdot \mathbf{u}_k = 0, \tag{2.1a}$$

$$\rho_k \left(\partial_t \mathbf{u}_k + \mathbf{u}_k \cdot \nabla \mathbf{u}_k \right) = \nabla \cdot \sigma_k + \rho_k \, \mathbf{g}, \tag{2.1b}$$

where $\mathbf{u}_k = \mathbf{u}_k(x, y, z, t)$ is the velocity vector in all three spatial directions, and the underscore $k = 1, 2$ denotes whether the equation holds for the air phase ($k = 1$) or the water phase ($k = 2$). A sketch of the situation is seen in figure 2.1. The density and the stress tensor in the two phases are denoted ρ_k and σ_k, respectively. $\mathbf{g}$ is the gravitational acceleration. For Newtonian fluids, the stress tensor is

$$\sigma_k = -p_k \mathbf{I} + 2\mu_k \mathbf{s}_k, \tag{2.2}$$

where, p_k is the pressure, μ_k is the dynamic viscosity and $\mathbf{s}_k$ is the strain rate tensor

$$\mathbf{s}_k = \frac{1}{2} \left(\nabla \mathbf{u}_k + (\nabla \mathbf{u}_k)^T \right). \tag{2.3}$$

Equations (2.1a), (2.1b) and (2.2) are referred to as the incompressible Navier–Stokes equations. In order to solve the equations, suitable initial and boundary conditions need to be assigned. In particular, interface conditions are needed to match the two phases.

A geometrical interface between different phases of a fluid may be described by the zero contour of the implicit function

$$G(x, y, z, t) = 0. \tag{2.4}$$

As an example, a simple propagating sine wave would be $G(x, y, z, t) = y - \sin(k(x - ct)) = 0$. The surface normal is given as

$$\mathbf{n} = \nabla G / |\nabla G|. \tag{2.5}$$

For viscous fluids, the velocities must be continuous across the interface

$$[\mathbf{u}]_G = 0, \quad \text{or equivalently:} \quad \mathbf{u}_2 = \mathbf{u}_1, \tag{2.6}$$

where we have used the convenient jump notation $[f]_G = f_2 - f_1$. Conservation of momentum dictates that the jump in stresses must be balanced by surface tension. This can be written as

$$\mathbf{n} \cdot [-p\mathbf{I} + 2\mu\mathbf{s}]_G = \sigma \kappa \mathbf{n}, \tag{2.7}$$

where σ is the surface tension coefficient and κ is the mean curvature of the interface. More details about the interface boundary conditions may be found in Åkervik & Vartdal (2016).

The numerical code used in this report employs a somewhat different approach to describe the problem mathematically. Instead of splitting the domain in two, a one-domain Navier–Stokes system on the form

$$\rho \left(\partial_t \mathbf{u} + \mathbf{u} \cdot \nabla \mathbf{u} \right) = \nabla \cdot \sigma + \rho \, \mathbf{g} + \mathbf{T}_\sigma, \tag{2.8}$$
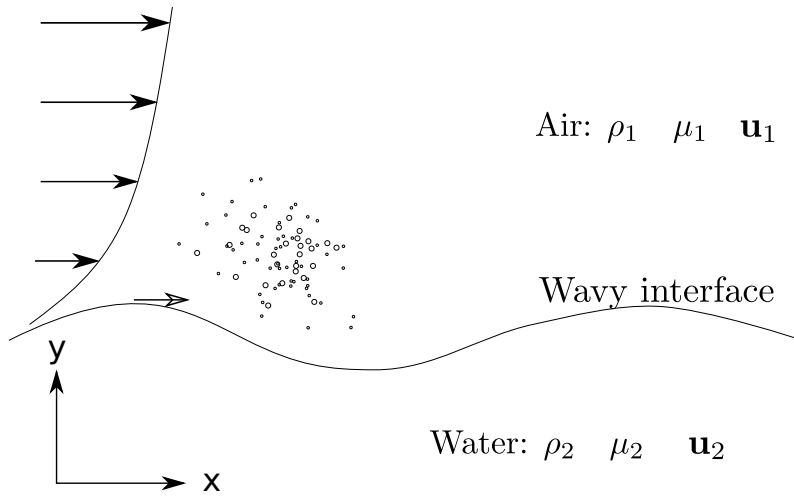
Figure 2.1   Illustration of the physical problem. In the air phase the density is ρ_1, the viscosity μ_1 and the corresponding velocities are $\mathbf{u}_1$. Below the air phase there is a water phase with density ρ_2, viscosity μ_2 and velocities $\mathbf{u}_2$. These two phases are separated by a wavy interface.

is used. Here, ρ and μ, and therefore σ, exhibit jumps across the interface. This can be stated by use of a Heaviside colour function C

$$C(G) = \begin{cases} 0, & G < 0 \\ 1, & G > 0 \end{cases}. \tag{2.9}$$

The resulting density and viscosity are written as

$$\begin{aligned} \rho &= C(G)\rho_1 + (1 - C(G))\rho_2, \\ \mu &= C(G)\rho_1 + (1 - C(G))\mu_2, \end{aligned} \tag{2.10}$$

where, as before, the subscript states the different phases of the fluid.

The action of the surface tension is accounted for by $\mathbf{T}_\sigma$ in equation (2.8). Generally, surface tension is important for short waves, but in the present case we omit its contribution to the force balance at the surface. Therefore, implicitly we exclude the effect of capillary waves.

2.2   Scaling and non-dimensional quantities

Due to the high resolution requirements needed to solve the equations for geophysical applications it is virtually impossible to solve the "full-scale" problem using the current high fidelity method. The high resolution requirements stems from the need to resolve both large scale phenomena as well as small scale phenomena. The largest scales in the flow are on the order of the boundary layer height ($\mathcal{O}(100 - 1000\,\mathrm{m})$), whereas the smallest scales are on the order of the smallest turbulent length scales ($\mathcal{O}(0.01 - 1\,\mathrm{mm})$). This scale separation is usually characterised by the Reynolds number

$$\mathrm{Re} = \frac{u_* h}{\nu}, \tag{2.11}$$

where u_* is a characteristic velocity scale of the large scale turbulent eddies, h is the corresponding length scale and ν is the kinematic viscosity. For turbulent boundary layers, a common characteristic velocity scale is the friction velocity, which is approximately 5% of the free-stream velocity (Pope, 2000). The corresponding length scale h may be taken as the largest turbulent eddy sizes, which scales as the boundary layer height h. The kinematic viscosity of air is $\nu \approx 1.5 \cdot 10^{-5}\,\mathrm{m^2/\,s}$. For a velocity scale of $u_* = 0.5$ m/s and an atmospheric boundary layer of depth $h = 1000$ m the Reynolds number is $\mathrm{Re} \approx 10^7$, which is virtually impossible to solve using high fidelity turbulence resolving methods. However, good insight into the behaviour of high Reynolds number turbulent boundary layers can be gained through reduced Reynolds number studies (see for instance Smits $et\ al.$, 2011).

The presence of water waves in the problem leads to a range of new non-dimensional numbers. The most important of these in the present context is the wave age (see for instance Donelan, 1998; Sullivan $et\ al.$, 2000; Åkervik & Vartdal, 2019)

$$c_* = c/u_*. \tag{2.12}$$

The wave age is the ratio of the phase velocity of the waves to the flow velocity. This parameter defines the state of the waves. For instance, the wind sea regime, where wind generate waves, occurs for approximately $c_* < 15$. Wave growth is more rapid and the sea is rougher at $c_* < 10$. On the other hand, the swell regime, where waves generate wind, occurs when $c_* > 15$.

The wave age is closely related to the Froude number, which is a well known quantity in comparing the effect of buoyancy and inertia. This can be seen from the relation

$$c_* = \frac{\sqrt{g/k}}{u_*} = \sqrt{\frac{\mathrm{Fr}^{-2}}{kh}}, \quad \mathrm{Fr} = \frac{u_*}{\sqrt{gh}}, \tag{2.13}$$

where deep water and large density contrast has been assumed, and kh is the ratio of the turbulent length scale to the wave length.

Another set of important parameters is the density and viscosity contrast in the two phases

$$r = \frac{\rho_2}{\rho_1}, \quad m = \frac{\mu_2}{\mu_1}. \tag{2.14}$$

The density contrast is important in quantifying the phase speed of waves propagating at the interface as well as to quantify the rate at which waves grow (Lamb, 1932; Miles, 1957). In the current problem of air flow over water waves, the density contrast is large ($r \approx 850$). This implies that the growth of waves is relatively slow and that the wave propagation speed is almost equal to a freely propagating wave. The viscosity contrast is important in determining the shear layer thicknesses in the two phases, and has an important effect on the wave characteristics. To perform numerical simulations of propagating waves, one has to assert that the wave Reynolds number

$$Re_w = c\rho_2/(k\mu_2) \tag{2.15}$$

is sufficiently large to avoid excessive viscous damping of the propagating wave (see for instance Åkervik & Vartdal, 2016). For the current set-up, with density and viscosity contrasts of $r = 850$ and $m = 60$, respectively, the criterion is

$$Re_w = \frac{c\rho_2}{k\mu_2} = \frac{c\,r\,\rho_1\,u_*\,h}{u_*\,kh\,m\,\mu_1} = \frac{r}{m}\frac{c_*\mathrm{Re}}{kh} = 14\frac{c_*\mathrm{Re}}{kh} \gg 1. \tag{2.16}$$

Hence, in the current coupled system, for a given wave length to boundary layer height and wave age, the requirement of a sufficiently high wave Reynolds number, leads to a requirement of a sufficiently high air-flow Reynolds number.

Propagating water waves also depend on the wave steepness (ak), where a is the wave amplitude. The wave steepness determines the degree of non-linear interaction between different wave lengths. For $ak > 0.2$, breaking waves may occur, whereas for $ak < 0.05$ there is hardly any transfer of energy between different wave lengths. Here we choose $ak = 0.1$, which will result in some transfer of energy that gives rise to Stokes waves, but breaking is not part of the dynamics. Furthermore, the shallowness parameter kd, with d being the water depth is important. As an example, tsunamis and tidal waves are so long ($kd \ll 1$) that their propagation velocity is determined by the water depth. In this report we use $kd = 2\pi$ for which the influence of the bottom is negligible.

With these considerations, one ends up with three essential non-dimensional numbers

$$\mathrm{Re} = \frac{u_* h}{\nu_1}, \quad \mathrm{Fr} = \frac{u_*}{\sqrt{gh}} \quad \text{and} \quad kh. \tag{2.17}$$

One important feature of this coupled flow, is that the Reynolds number and the Froude number are not independent quantities. As a result, once these two are fixed, the physical velocities and lengths are fixed:

$$u_* = \left(g\,\mathrm{Re}\,\nu\,\mathrm{Fr}^2\right)^{1/3}, \quad h = \left(\frac{\mathrm{Re}^2\,\nu^2}{g\,\mathrm{Fr}^2}\right)^{1/3}, \tag{2.18}$$

where μ is the kinematic viscosity and g is the gravitational acceleration. It is therefore not possible to match full scale Reynolds numbers and Froude numbers simultaneously at laboratory scales unless viscosity is altered. Consider for instance the atmospheric flow with scales $u_* = 0.5\,\mathrm{m/s}$, $h = 100\,\mathrm{m}$ over water waves with a wave length of $\lambda = 100\,\mathrm{m}$ ($k = 2\pi/\lambda = 0.063\,\mathrm{m}^{-1}$). This yields

$$\mathrm{Re} = \frac{u_* h}{\nu} = 3.3 \cdot 10^6, \quad \mathrm{Fr}^{-2} = \frac{gh}{u_*^2} = 3924, \quad \text{and} \quad kh = 6.3 \quad \Rightarrow \quad c_* = \sqrt{\frac{\mathrm{Fr}^{-2}}{kh}} = 25. \tag{2.19}$$

The wave age of $c_* = 25$, corresponds to a swell regime (Åkervik & Vartdal, 2019). Suppose we are to study this air-water system in a wind-wave experimental facility, where the physical dimensions of the laboratory limits the boundary layer height to $h = 10\,\mathrm{m}$. The Reynolds number can be matched for the same viscosity using $u_* = 5\,\mathrm{m/s}$ (which is a very high friction velocity). If also the wave length is reduced by a factor of ten, we get $k = 0.62\,\mathrm{m}^{-1}$ and

$$\mathrm{Re} = \frac{u_* h}{\nu} = 3.3 \cdot 10^6, \quad \mathrm{Fr}^{-2} = \frac{gh}{u_*^2} = 3.924, \quad \text{and} \quad kh = 6.3 \quad \Rightarrow \quad c_* = \sqrt{\frac{\mathrm{Fr}^{-2}}{kh}} = 0.8.$$
$$\tag{2.20}$$

The resulting wave age is much smaller than in the full scale problem. Hence, for a fixed Reynolds number, one ends up studying wind waves instead of swell waves. Therefore, it is necessary to lower the Reynolds number in the wind tunnel to achieve the same wave age.

In numerical simulations, it is the computational resources required that limits the Reynolds number. Thus, given a finite amount of computational resources, high fidelity numerical simulations often (but not always) deals with the study of small length scales. The hope is that the dynamics present on small length scales is important also on atmospheric scales.

In the present, work we scale the problem with the boundary layer height h and the friction velocity u_*. This results in the momentum equations

$$\bar{\rho}\left(\partial_t \mathbf{u} + \mathbf{u} \cdot \nabla \mathbf{u}\right) = \nabla \cdot \sigma + \bar{\rho}\mathrm{Fr}^{-2}, \quad \sigma = -p\mathbf{I} + 2\bar{\mu}\mathrm{Re}\,\bar{\mathbf{s}} + \sigma_{sgs}. \tag{2.21}$$

Here, the non-dimensional density $(\bar{\rho}(x, y, t))$ and viscosity $(\bar{\mu}(x, y, z, t))$ are given as

$$\bar{\rho} = C(G) + (1 - C(G))r \quad \text{and} \quad \bar{\mu} = C(G) + (1 - C(G))m. \tag{2.22}$$

In the air phase, where $C = 1$, $\bar{\rho} = 1$ and $\bar{\mu} = 1$, whereas in the water phase, where $C = 0$ $\bar{\rho} = r$ and $\bar{\mu} = m$. Unresolved turbulent fluctuations are modelled as the stress tensor σ_{sgs}. The effect of buoyancy is accounted for by the Froude number $\mathrm{Fr} = u_*/\sqrt{gh}$. Since we are studying the effect of wave age on the transport characteristics, we vary the wave age by varying the Froude number while keeping the depth parameter kh and the Reynolds number constant. This approach can be justified based on the importance of the wave age in this flow.

2.2.1   Equations of motion for particle transport

The aerosol transport characteristics is studied using a Lagrangian particle method, where particles are transported with the flow. The non-dimensional mass of a particle is given as

$$m_p = \frac{\rho_p \frac{1}{6}\pi d_p^3}{\rho_a} = \bar{\rho}_p \frac{1}{6}\pi d_p^3, \quad \bar{\rho}_p = \rho_p/\rho_a, \tag{2.23}$$

where $\bar{\rho}_p$ is the density of the particle relative to air density and d_p is the non-dimensional particle diameter. The location of a particle, denoted $\mathbf{x}_p = (x_p, y_p, z_p)$, is given by the first order differential equation

$$d_t \mathbf{x}_p = \mathbf{v}_p, \tag{2.24}$$

where the particle velocity is $\mathbf{v}_p = (u_p, v_p, w_p)$. The particle velocity is governed by the second law of Newton

$$m_p d_t \mathbf{v}_p = \mathbf{F}, \tag{2.25}$$

where $\mathbf{F} = (F_x, F_y, F_z)$ are the forces acting on the particle in the three directions of space. Generally, the forces may be subdivided into three categories, namely those of fluid-particle interaction forces, particle-particle interaction forces and body forces such as gravity. In the present work, gravitational settling is omitted. If we were to include this effect, gravitational settling would lead to deposition on the surface for the larger particles. The main reason for excluding the effect of gravitational settling, is that we seek to isolate the mechanisms related to inertial forces in the flow. However, on real scales, and for particles of some size, this term has to be included. Particle-particle interaction is also an interesting topic, but on atmospheric scales, mixtures are typically dilute. Forces stemming from the fluid flow are i) background fluid shear and pressure forces, *i.e.* which are present also in the absence of particles, ii) inviscid history or apparent mass terms, iii) viscous history terms and iv) steady state drag. In the present work, we only consider the steady state drag. If gravity settling was active, or if the particles were large, one would need to include the background pressure forces in order to ensure hydrostatic balance. Whenever there are large differences in the acceleration between the fluid and the particles, and the fluid is dense, particles will be subject to apparent mass effects. If at the same time, the fluid has high viscosity, on may also need to include viscous history effects. Keeping only the steady state drag we end up with

$$\mathbf{F} = \frac{1}{2}\bar{\rho}C_{\mathrm{D}}\frac{\pi d_p^2}{4}\left|\mathbf{u} - \mathbf{v}_p\right|\left(\mathbf{u} - \mathbf{v}_p\right), \tag{2.26}$$

where $\bar{\rho}$ is the non-dimensional fluid density as given in equation (2.22). The drag coefficient C_D is taken from Schwarzkopf *et al.* (2012)

$$C_d = \frac{24}{\mathrm{Re}_p} \left[1.0 + 0.15 \mathrm{Re}_p^{0.687} + 0.0175(1 + 4.25 \times 10^4 \mathrm{Re}_p^{-1.16})^{-1} \right]. \tag{2.27}$$

The particle Reynolds number Re_p is given as

$$\mathrm{Re}_p = \mathrm{Re}|\mathbf{u} - \mathbf{v}_p| d_p \, \bar{\rho}/\bar{\mu}. \tag{2.28}$$

From this expression it can be seen that the particle Reynolds number scales linearly with fluid Reynolds number. Furthermore we observe that since $d_p \ll 1$, the particle Reynolds number is usually much smaller than the fluid Reynolds number.

2.2.2 The time scales of the flow and the particle motion

Small and light particles adapt easily to changes in the flow field, and therefore passively follow the turbulent flow. Large and heavy particles have more inertia, and need time to adjust to the flow field. One quantity that describe this feature is the Stokes number, which is a measure of the inertia of the particles compared to the inertia imposed by the flow. This ratio can be expressed as the ratio of two time scales

$$\mathrm{St} = \frac{\tau_p}{\tau_{\mathrm{flow}}}, \tag{2.29}$$

where τ_p is the time scale of the response of the particle to the drag force imposed by the flow, and where τ_{flow} is some time scale of the flow.

Traditionally, the time scale of the particle is based on the Stokes flow assumption (low Reynolds number, *i.e.* small length scales, velocities and/or highly viscous fluids) and reads in non-dimensional form

$$\tau_p = \frac{\bar{\rho}_p d_p^2 Re}{18\bar{\mu}}, \tag{2.30}$$

In this assumption, viscous forces dominate, which is typically the case for very low velocities or for very viscous fluids.

Figure 2.2 (a) shows the response time for the current setup with $\bar{\rho}_p = 850$, $Re = 395$ and $\bar{\mu} = 1$ for different particle sizes. Clearly, particles with a diameter of $d_p = 10^{-2}$ or larger will respond very slowly to flow changes. For instance, for the case of a particle diameter of $d_p = 10^{-2}$, the Stokes time scale is $\tau_p = 1.9$. The time scale of the wind (swell) wave is $1/(ck) \approx 0.05$ (0.008), which is clearly much faster than the Stokes time scale. There are numerous time scales available in the flow itself. One time scale is the time it takes for the mean flow to transport structures over one wave length

$$\tau_A = 1/(kU(y)), \tag{2.31}$$

In the free stream, this timescale is very small, whereas close to the surface this timescale becomes large. Another important time scale is associated with the large scale turbulent motion, often referred to as the eddy turnover time. This may be written in terms of the turbulent kinetic energy

$$\tau_E = y/\sqrt{|u'^2|}, \tag{2.32}$$

where $|u'^2|$ is the streamwise component of the turbulent kinetic energy. Another possible estimate for the eddy turnover time is the strain rate magnitude of the flow

$$\tau_s = 1/|s|, \quad |s| = \sqrt{\mathrm{tr}(\mathbf{s}^T \mathbf{s})}. \tag{2.33}$$
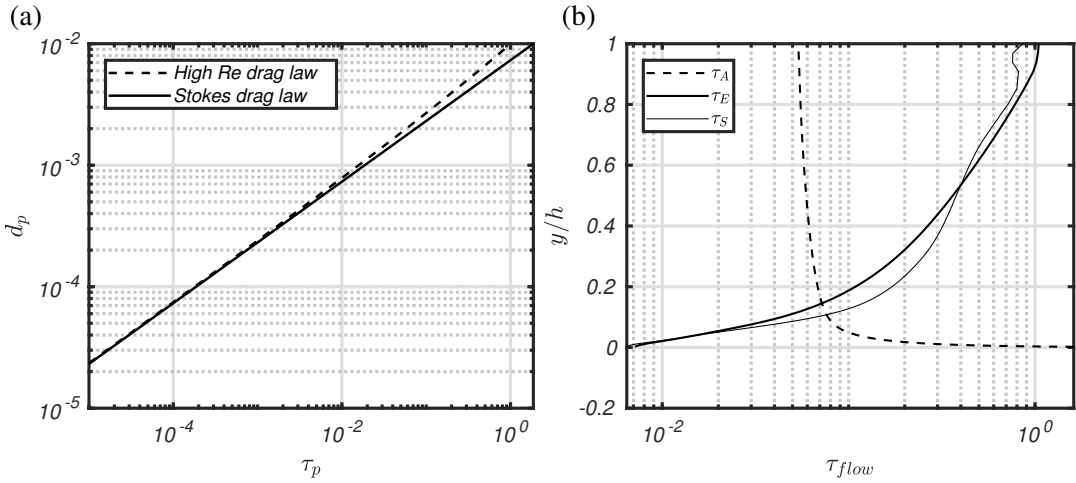
Figure 2.2 *(a) Particle time scale versus particle diameter $\bar{\rho}_p = 850$, $\bar{\mu} = 1$ and $Re = 395$,*
(b) flow timescale taken from case I for $c/u_* = 2$, i.e. one phase simulations.

The two latter are approximate measures of the time scales inherent to the largest eddies and grows with distance from the surface, since as the distance to the surface is increased, so will the permitted size of the eddies. Figure 2.2 (b) shows the time scales obtained from the three measures for case II in table 3.1 with $c/u_* = 2$. Close to the surface, τ_E and τ_s are almost identical. In the region $y < 0.1$, either of these will give the approximate smallest energy containing time scale in the flow. Above this, the figure shows that τ_A is smaller. Keeping in mind that τ_A is a measure of the time it takes to transport a structure over one wave length, it implies that above $y \approx 0.2$ mean shear straining of turbulent eddies is slow compared to advection with the mean flow (Belcher & Hunt, 1993).

By comparing figure 2.2 (a) and (b), we see that in the outer part of the flow, a unity Stokes number (St $= \tau_p/\tau_{flow} = \tau_p/\tau_A$) is obtained for particles with $d_p \approx 2 \cdot 10^{-3}$ since $\tau_A \approx 5 \cdot 10^{-2}$. This implies that smaller particles will act as passive tracers, whereas larger particles will respond slowly to changes in the flow. Close to the surface, the smallest time scale of the flow is given by $\tau_{flow} = \tau_s \approx 10^{-2}$, which implies that unity Stokes number is achieved for $d_p \approx 5 \cdot 10^{-4}$.

3   Simulations

The Navier–Stokes equations (2.21) are solved by means of Large eddy simulation (LES), using an unstructured finite-volume node-based solver from Cascade Technologies (see for instance Ham *et al.*, 2006, 2007). LES sub-grid terms are modelled by means of a dynamic Smagorinsky procedure suitable for unstructured grids, as described in Mahesh *et al.* (2004). In the single-phase version VIDA, the equations are advanced in time using the second order BDF-2 scheme, and a fractional step predictor-corrector procedure is employed to ensure conservation of mass. The two-phase VoF solver is an extension of VIDA, and the basics are schematically described in Kim *et al.* (2014). The VoF-based scheme is fully conservative and un-split, allowing exact mass conservation and robust handling of high density ratios. Prior to advection of momentum, the geometry of the interface is reconstructed based on the Piecewise Linear Interface Calculation (PLIC) scheme (Ashgriz & Poo, 1991; Parker & Youngs, 1992). The PLIC scheme has the advantage of being able to conserve mass, while maintaining a monotone advection scheme. This property is important for the current problem, since we need to ensure that the dispersion relation of the propagating waves are not destroyed. In Åkervik & Vartdal (2016) we showed that the current VoF scheme is indeed able to preserve the dispersion relation of propagating waves.

3.1   Flow setup

Table 3.1 shows the details of the different simulations. All simulations are performed on rectangular box domains where the streamwise direction is x, the vertical direction is y and the crosstream direction is z. Uniform grid spacing is employed in the streamwise and crosstream directions. In the vertical direction, where small scales structures at the interface needs to be captured, a geometric stretching of the grid is performed. All cases are driven by a volume force (which in nondimensional form is unity) and the streamwise and crosstream directions are taken to be periodic.

For the VoF simulations (Ia and Ib), we first initialise the turbulence in the air phase by means of interpolation from a one-phase air simulation that spans a vertical domain of $y \in [0, 1]$. In the one phase simulation, the flow is initialiazed with a laminar analytic Poiseuille profile. This laminar flow field naturally undergoes transition to turbulence. Once a statistically stationary turbulent field is obtained, the flow field is interpolated to a two-phase domain that span $y \in [-1, 1]$. Consequently, the water column is quiescent. At the interface and in the water column a linear Airy-wave (Lamb, 1932) is introduced at t=0, *i.e.*

$$G(x, y, z, t = 0) = y - a\sin(kx), \quad \text{interface located at } G = 0 \tag{3.1}$$

$$u(x, y, z, t = 0) = ak\, c\exp(ky)\sin(kx), \quad G > 0 \tag{3.2}$$

$$v(x, y, z, t = 0) = -ak\, c\exp(ky)\cos(kx), \quad G > 0. \tag{3.3}$$

$$\tag{3.4}$$

Here, G is the distance to interface function described above. This function is positive (negative) in the water (air) phase and zero at the interface. The above initial condition will introduce a transient in the flow, since the boundary layer flow is not in balance with the imposed propagating wave. Consequently, for all cases we let the system stabilise before particles are injected. We found that balance was achieved after five flow throughs ($th/U_\infty \approx 5$). As seen in table 3.1, three flow regimes are considered. These are; the flat boundary layer case ($ak = 0$, $c/u_* = 0$), a wind sea case ($ak = 0.1$, $c/u_* = 2.8$) and a swell case ($ak = 0.1$, $c/u_* = 19.9$).

	Case	Type of simulation	L_x	L_z	y_{min}	y_{max}	r	m	Re	c/u_*
PHYSICAL	Ia	Two phase (air-water)	6	6	-1	1	850	60	395	Flat
	Ib	Two phase (air-water)	4	4	-1	1	850	60	395	2.8, 19.9
	II	One phase (air)	6	3	$a\sin(kx)$	1			395	2, 16

	Case	N_x	N_z	N_y^{air}	N_y^{water}	$\Delta^+ x$	$\Delta^+ z$	Δy^+_{min}	Δy^+_{max}	Δy_{growth}
NUMERICAL GRID	Ia	200	200	80	80	11.9	11.9	0.8	15.6	1.04
	Ib	160	160	80	80	9.9	9.9	0.8	15.6	1.04
	II	250	150	94		9.5	7.9	0.8	12.4	1.03

Table 3.1 Computation cases. All cases use a geometric stretching in the vertical direction of $r = 1.03$. The two first cases are Volume of Fluid simulations, whereas the last one is a single phase air simulation. The upper panel shows the physical parameters and the lower shows the numerical details.

In previous work, we have discussed the role of wave age and Reynolds number in a one phase setting for this flow (Åkervik & Vartdal, 2019). In the one phase setting, only the air flow is considered - the presence of the wave is accounted for by introducing a propagating wave at the lower boundary according to equation (3.1) with $G = 0$. Since the density contrast is large ($r = 850$) for the air-water system, the waves will react slowly to the imposed air flow. As a result, wave growth/decay is rather slow, and the propagating wave will preserve its shape for a sufficiently long time window to gather turbulent statistics. This justifies the use of a one-phase model. In Åkervik & Vartdal (2019), it was shown that for low wave ages, *i.e.* in the wind sea regime, there is a large sensitivity in turbulent and wave correlated stresses with both wave age and Reynolds number. On the other hand, when entering the swell wave regime ($c/u_* > 12$) the flow tends towards simple behaviour, dominated by the fast wave propagation. In this work, we will use some of these results to visualise the key features of the flow over waves. This is referred to as case II in table 3.1.

3.2 Initial particle distribution

All three cases are initiated with the particle distribution shown in figure 3.1. Initially we performed the simulations in case Ia in table 3.1 with the particle sizes $d_p = \{10^{-5}, 10^{-3}\}$ for the flat case, the wind sea case and the swell case. For each particle size, six individual puffs consisting of $N_p = 25000$ particles are released at the initial time. The locations of these puffs are $x_p^0 = 0.2$, and $z_p^0 = \{0.5, 1.5, \ldots, 5.5\}$. This spacing in the crosstream direction is used to ensure that the individual puffs are not trapped in the same turbulent eddy. In this way, the statistical representability of the plume development is improved. One weakness with this setup, is that the puffs are released at one downstream location. This renders it likely for particles to be trapped in the vortices related to the wave correlated motion. Especially for the swell case of $c/u_* = 19.9$ this may be problematic. To address this problem, we performed simulations for both the wind sea and the swell case with particle location distributed over one wave length ($x_p^0 = \{0.25, 0.5, 0.75, 1\}$) at crosstream locations $z_p^0 = \{0.5, 1.5, 2.5, 3.5\}$. To save computational costs, the domain size was reduced. The reduction in domain size from $L_x = L_z = 6$ to $L_x = L_z = 4$ should be unproblematic, since the correlation lengths in this type of flow are substantially smaller (Yang & Shen, 2009).

For the flat case, the particle sizes $d_p = \{10^{-5}, 10^{-3}\}$ were considered, whereas for the swell case we additionally considered $d_p = 3 \cdot 10^{-4}$. As we will see later, in the wind sea case, deposition
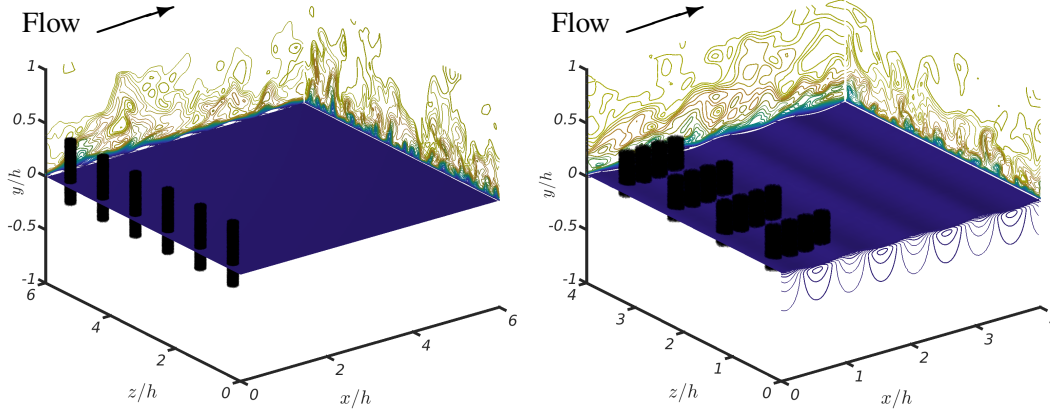
Figure 3.1   Initial set up of puff simulations.   The black dots show the initial particle distribution. The blue surface is the interface between air and water, and the colour contours shows the initial streamwise velocity in the air phase and the water phase for the low wave-age case. Left: Case Ia: Larger domain and cylinder-shaped distribution of particles centred at $x = 0.2$ and at the spanwise locations $z = \{0.5, 1.5, \ldots, 5.5\}$. This is used for the flat simulation. Right: Smaller domain and cylinder-shaped distribution spread over one wave length, $x = \{0.25, 0.5, 0.75, 1\}$ and at spanwise locations $z = \{0.5, 1.5, 2.5, 3.5\}$. This is used for the wave simulations.

is frequent. Therefore, the particle sizes $d_\mathrm{p} = \{10^{-5}, 3 \cdot 10^{-4}, 6 \cdot 10^{-4}, 8 \cdot 10^{-4}, 10^{-3}, 1.2 \cdot 10^{-3}\}$ were considered for the wind sea case in order to illustrate how deposition depends on Stokes time scale.

3.3   Deposition and escaping the computational domain

Some particles are deposited at the surface, whereas others are able to leave the domain at the top boundary. In the current work, we keep track of both of these events. The escape rate was found to be approximately 2% per unit time.

The criterion to decide if a particle has deposited is fairly straightforward. Each particle is tagged with the fluid property of the surrounding fluid, *i.e.* density, viscosity and velocity of the surrounding fluid is interpolated to the particle position. This means that a particle located in the water column will experience a nondimensional density of $\bar\rho$. If a particle is in the vicinity of the surface the density will be in the range $1 < \bar\rho < r$. To evaluate deposition, we flag particles where $\bar\rho > 20$. Then the time series of that particle is checked to see if that particle has in fact deposited ($\bar\rho \approx r$).

3.4   Concentration

In the current set-up, the release consists of individual particles that are tracked in time and space, *i.e.* a Lagrangian approach is used. This makes it challenging to define a concentration. One possible approach is to define a Cartesian grid centred around the plume and count the number of

particles within each volume. We have used a more refined method that involves Voronoi diagrams, where the volume around each particle is computed. This volume is occupied by locations in space that are closer to the current particle than they are to any other particle. In this manner, the Voronoi cells represents the volume occupied by each particle. This method is more automated than the Cartesian grid method. For densely/sparsely packed particles, the volume occupied by each particle is small/large. The concentration may hence be obtained as the inverse of the volume. The interested reader is directed to Barber *et al.* (1996) for details on how this procedure works, but in the present work we used the `MATLAB` builtin capability `voronoin` to build the Voronoi diagram and `convhull` to compute of the corresponding volumes.

3.5   Measure of plume location

To obtain a quantitative measure of the plume location the following procedure was introduced: The data at each instance in time was sorted according to increasing streamwise, crosstream and vertical coordinate. Subsequently, in each direction the location of the 10th percentile and the 90th percentile was calculated. To ensure that these statistics represent air concentrations, particles deposited in the water column and particles that originates from the water phase are excluded from these statistics. The current method serves as a crude measure to locate the core and edges of the plume. The definitions of arrival time and spread angle use this metric. More specifically, we denote the arrival time as the time when the 90 percentile has reached a specific location. Note that the concentrations in the previous section (section 3.4) does not need to be corrected for water phase particles. The reason for this is that the Voronoi diagram calculates local concentrations.

4 Results

4.1 Mean flow description

Figure 4.1 shows (a) the mean flow, (b) the streamwise (c) crosstream stresses, (d) the shear stresses and (e) the vertical strain rate for the three cases (Ia and Ib in table 3.1) as black lines. The blue lines show the crest and through height levels for the wave cases. Note that the stresses in this context is the sum of both the turbulent stresses and the wave correlated stresses. To see this, one may decompose the velocity fields as follows

$$u(x, y, z, t) = \bar{u}(y) + u_w(x, y) + u'(x, y, z, t), \quad v(x, y, z, t) = \bar{v}(y) + v_w(x, y) + v'(x, y, z, t), \quad (4.1)$$

where $\bar{\cdot}$ denotes averaging in time and the lateral directions. Here, $\bar{u}$ is the vertical profile of the mean streamwise velocity, u_w is the streamwise wave correlated mean flow field (laminar), which varies in the streamwise direction and the vertical direction, and $u'(x, y, z, t)$ is the streamwise component of the turbulent flow field. In this respect, the mean flow over waves differ from the flow over a flat surface - in the flow over waves, the mean flow consist of a background mean and a wave correlated/induced mean. The streamwise stress is defined as

$$\overline{(u(x, y, z, t) - \bar{u})(u(x, y, z, t) - \bar{u})} = \overline{(u_w + u')(u_w + u')} = \overline{u_w u_w} + \overline{u' u'}, \quad (4.2)$$

and likewise the shear stress is

$$\overline{(u(x, y, z, t) - \bar{u})(v(x, y, z, t) - \bar{v})} = \overline{(u_w + u')(v_w + v')} = \overline{u_w v_w} + \overline{u' v'}. \quad (4.3)$$

Effectively this means that the flow over waves experience both turbulent and wave induced stresses. The mean flow for the flat surface case (--), the wind sea case (—) and the swell case (-•-) is shown in figure 4.1 (a). The wind sea case is subject to aerodynamic drag from the slow moving wave. Consequently, the mean flow is slightly lower than in the two other cases. For the swell case, the aerodynamic drag is negative, but this does not lead to a significant increase in mean flow compared to the flat surface case (--). Notice that for all cases, the mean flow at $y = 0$ is slightly positive. This is due to the surface drift created by the average drag exerted by the wind on the surface. For the streamwise stresses in figure 4.1 (b), we see in the water column that there is an increase of stress with increasing wave speed, since the wave motion is described by $(u, v) = ak\,c \exp(-k|y|)(\sin(kx - \omega t)), -\cos(kx - \omega t))$. On the air side the largest amplitude of the streamwise stresses is encountered for the swell case. This is entirely due to the fast propagating wave and not turbulence. Interestingely, the wind sea case has a significantly larger crosstream component (figure 4.1 (c)), which may lead to increased crosstream transport. For the shear stresses in figure 4.1 (d), all cases have zero stress in the water column. This is expected, since the streamwise and vertical velocities of a plane propagating wave are uncorrelated (or 90° out of phase). On the air side we observe that the largest shear stress is encountered for the wind-sea case, and the smallest is encountered for the swell case. The strain rate seen in figure 4.1 (e) shows that on average, the flat surface case has the highest amplitude, whereas the two wavy cases display similar behaviour. To gain more insight into the flow, one may separate the turbulent motion from the wave correlated motion. We will use the one phase results (II in table 3.1) for $c/u_* = 2$ and $c/u_* = 16$ to vizualise these effects. These results are based on simulations in Åkervik & Vartdal (2019).

Figure 4.2 shows the turbulent (a-b) and the wave correlated (c-d) shear stresses. The left panels of the figure (a and c) shows the low wave age (wind sea), whereas the right panels (b and d)
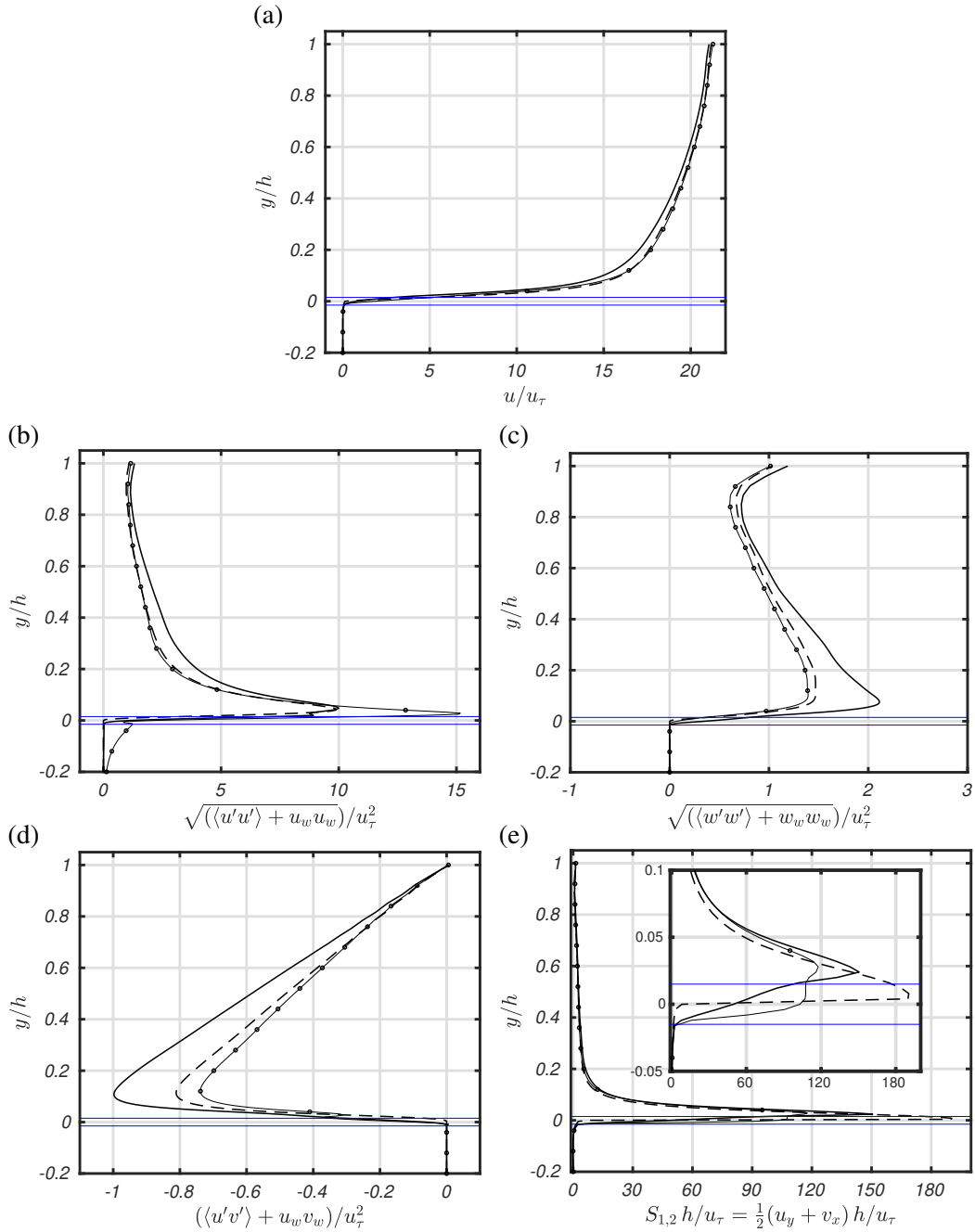
Figure 4.1 Vertical velocity statistics profiles: (a) Mean flow, (b) streamwise stress, (c) vertical stress, (d) turbulent shear stress and (e) strain rate, i.e. proportional to viscous shear stress. The inset in (e) shows a zoom close to the surface. Horisontal blue lines indicate the location of wave crest and trough for wavy cases. The different lines are: Flat surface (--), wind sea (—) and swell (-•-).
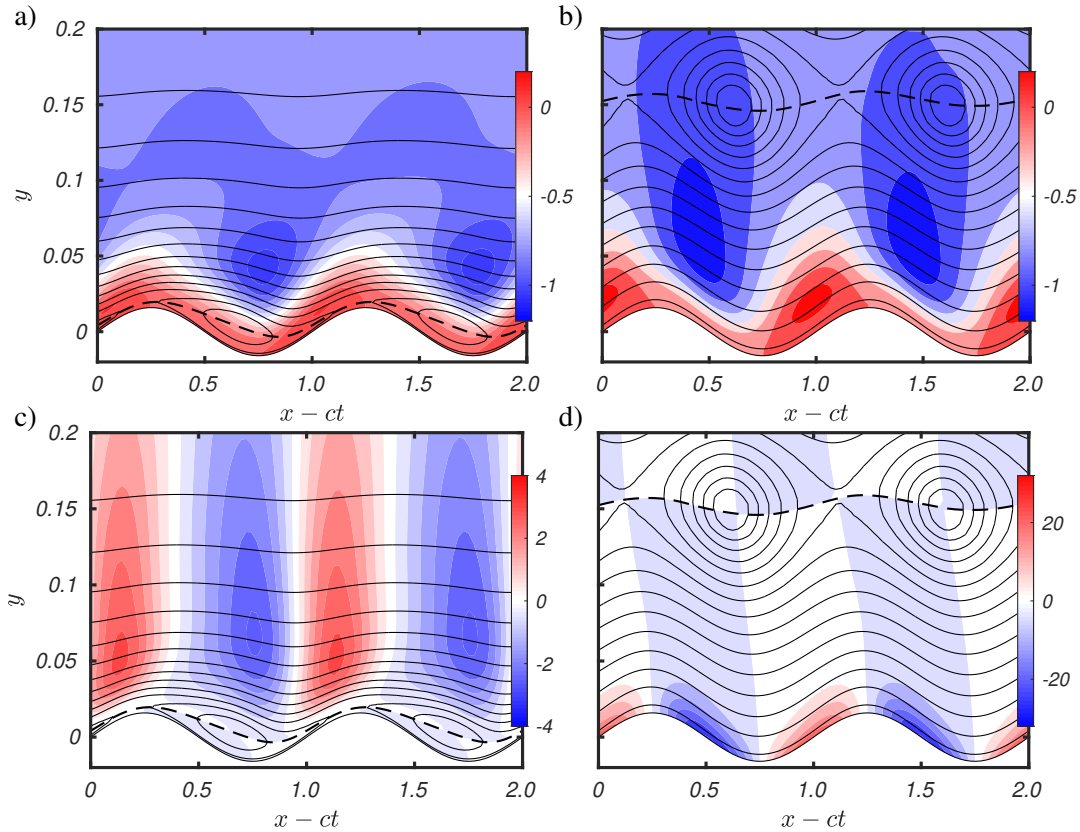
Figure 4.2 *Streamlines of flow together with Reynolds shear stress (a-b) and wave induced shear stress (c-d). a) and c) show wind sea conditions ($c/u_* = 2$) and b) and d) show swell sea conditions ($c/u_* = 16$). Results are taken from one-phase simulations. Notice that for the high wave-age case, the wave induced stresses (d) has a much higher amplitude than the corresponding Reynolds stresses (b). As a result, close to the surface the vertical transport is dominated by the wave induced stresses.*

shows the high wave age (b and d). The black contours in all frames shows the streamlines of the flow, whereas the dashed line shows the location of the critical layer (Miles, 1957), *i.e.* where the streamwise mean flow equals the phase speed of the waves. Above this, the mean flow is faster than the phase speed of the waves, whereas below this it is slower. As a consequence, fluid particles will circulate in a clockwise fashion around these so called cat's eyes. For the wind sea regime (low wave age) this circulation region is located close to the surface and therefore represent an essential part of the dynamics of the near surface region. In this region there is a complex interaction between the wave-correlated stresses, Reynolds stresses and viscous stresses. For swell waves (high wave age), this circulating region is located far from the surface, and although it is still active, it occupies a region where only turbulent stresses are active.

For the low wave-age case (a and c), the turbulent shear stress (a) has a negative peak above the through of the wave. This negative peak coincides with the negative peak in the wave induced shear stress (c). These two mechanisms locally cooperate to create a downward flux of momentum. Notice that the wave-induced stress has a higher amplitude than its turbulent counterpart. Naively one might expect that the wave-induced stress should give zero contribution when integrated over a
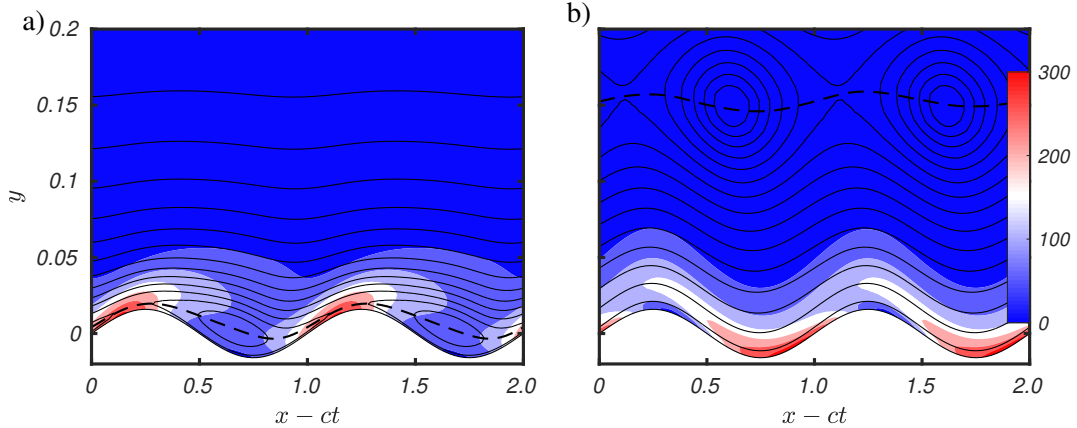
Figure 4.3   Streamlines of flow together with strain rate for a) wind sea conditions ($c/u_* = 2$) and b) swell sea conditions ($c/u_* = 16$). Results are taken from one-phase simulations. For $c/u_* = 2$ the so called cat's-eyes are located close to the surface, whereas for $c/u_* = 16$ they are located in the free stream.

wave length. However, due to viscous adjustment of the streamwise wave-induced velocity in the air, there is a phase shift which creates a strong correlation between the streamwise and vertical wave-induced velocity. On average this results in a downward flux, similar to the turbulent shear stress. Thus, wave-induced stresses enhance the downward momentum flux imposed by turbulence. For the swell case (b and d) there is also a strong wave correlation in the turbulent shear stress, but here the negative peak has moved upwind towards the wave crest and is located closer to the surface. For this case, there is a vertical separation of the regions where turbulent stresses are active, and where wave-induced stresses are active. The large amplitude in the wave-induced stress compared to the turbulent stresses indicates that close to the surface the wave-induced stresses dominate the dynamics of the flow.

Figure 4.3 shows the strain rate, or mean flow gradient, for the two wave ages. The streamlines are the same as in figure 4.2. Clearly, the mean flow gradient is large near the surface. For the low wave-age case (a) its peak is located just upstream of the wave crest, whereas for the high wave-age case it is located slightly downstream of the through. The inverse of the strain rate is commonly used as a measure of the time scale of the flow. For the low wave-age case the peaks are located at the horisontal edges of the critical layer. Since a large strain rate is indicative of small time scales of the flow, we would expect that finite size particles that are transported with the flow may leave the streamlines in these regions.

4.2   Evolution of puffs

Figure 4.4 shows the evolution of the puffs for particle size $d_p = 10^{-5}$ for the flat case (a,b), the low wave-age case (c, d) and the high wave-age case (e, f). The left column shows the vertical xy-plane (a,c,e), whereas the right column shows the horisontal xz-plane (b,d,f). The puffs are seen as point clouds of particles coloured by concentration, where dark red is unity concentration ($c = 1$), as seen at $t = 0$. As the particles are transported by the airflow, lower concentrations are seen, with bright red signifying $c = 10^{-2}$ and bright yellow signifying $c = 10^{-4}$. Also seen in the figure are areas where 80% of the particles in the different directions are located, *i.e.* the crosses show the 10th
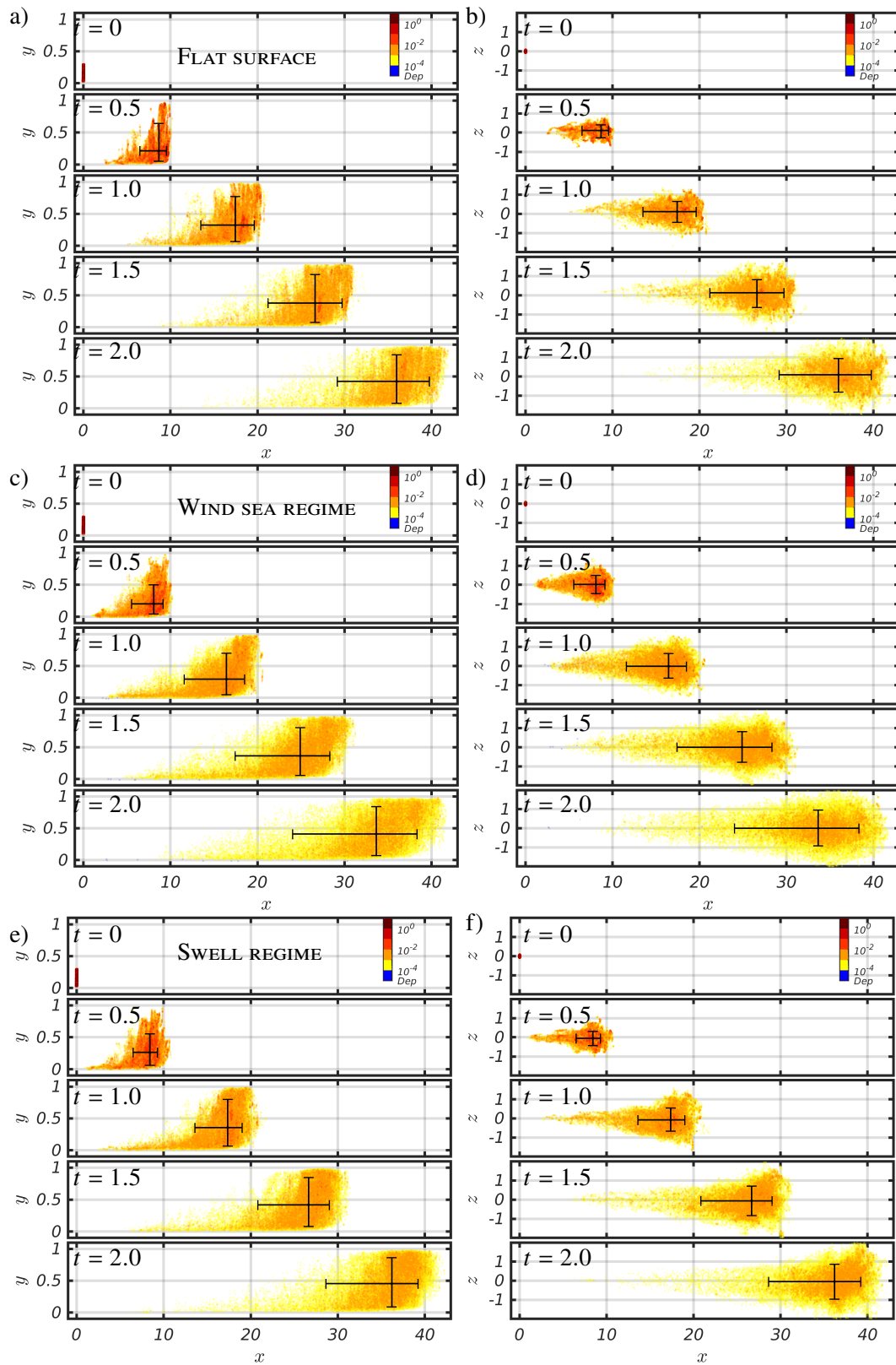
*Figure 4.4   Time evolution of particle distribution for particle size $d_\mathrm{p} = 10^{-5}$. a), c) and
e) show the $x - y$ plane, whereas b), d) and f) show the $x - z$ plane, for the flat
case (a,b), wind driven waves (c,d), swell waves (e,f). The dots show particles
coloured by concentration, where blue signifies deposition. For particles of this
size, deposition does not occur. The crosses denote the areas where in each
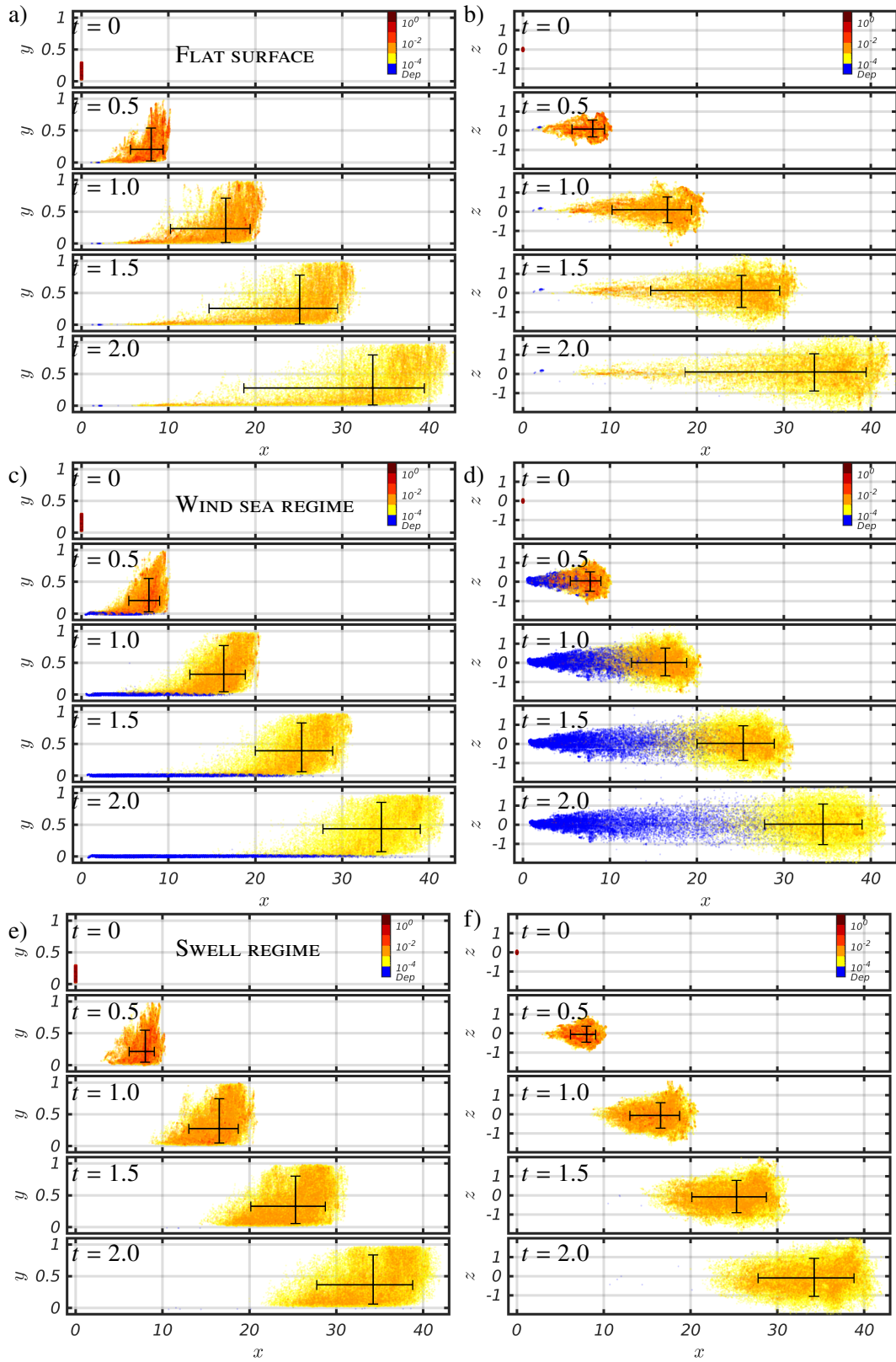direction 80% of the particles are located.*

FFI-RAPPORT 22/02547

Figure 4.5   Time evolution of particle distribution for particle size $d_p = 10^{-3}$. a), c) and e) show the $x - y$ plane, whereas b), d) and f) show the $x - z$ plane, for the flat case (a,b), wind driven waves (c,d), swell waves (e,f). The dots show particles coloured by concentration, where blue signifies deposition. The crosses denote the areas where in each direction 80% of the particles are located.

percentile to the 90th percentile. This serves as a crude statistical measure to characterise the plume.

Initially all particles are located within a cylinder type of shape. As time evolves and the puffs are transported downstream with the air flow, the plume stretches both laterally (as seen in b, d and f) and vertically (as seen in a, c and e).

From the figure one can observe (by the crosses and the point cloud) that the arrival time and plume spread is similar for all cases. For these smaller size particles, the wind sea creates a longer plume in the streamwise direction, probably due to and increased downward transport of particles which renders their transport slower. For these small particles there is no deposition on the surface.

Figure 4.5 shows the evolution of the puffs for particle size $d_p = 10^{-3}$. As for the smaller sized particles, the arrival time is similar for all cases. However, in this case it is the flat case that has the longest streamwise extent of the plume, whereas the two others have a more "puff" shaped footprint. The most noticeable feature for these larger particles, is the significant degree of deposition occurring for the wind sea case. This can be seen as blue dots in the surface region of figure 4.5 (c and d). It is well known that there is an increased downward momentum transfer in the wind sea regime. As we will briefly discuss later, this feature is related to the presence of a critical layer close to the surface. In this region, fluid particles are trapped in orbits following the propagating wave. While this is a clearly defined region in laminar flow (or in terms of mean flow), the instantaneous velocity in a turbulent flow will only mildly adhere to this dynamic. Regardless of this, the critical layer constitutes a region for which the flow above and below are unable to communicate properly. Particles that enter this region may end up being trapped for a considerable amount of time. When particles are sufficiently large to not simply passively follow the flow, this may give rise to a high degree of deposition. For the current case, more than 30% of the particles has deposited at $t = 1.5$. This is a large number, and the effect on the statistics is severe for the low wave-age case. This clear difference between the two particle sizes ($d_p = 10^{-5}$ and $d_p = 10^{-3}$) is in line with the discussion in section 2.2.2.

The flat case leaves particles close to the surface, but almost none are deposited. This is due to the absence of vertical motion close to the surface, and is a manifestation of the turbophoresis effect (see for instance Sardina *et al.*, 2012), where particles accumulate in regions with lower levels of turbulence. On the other hand, for the swell case, the turbophoresis effect appears to be counteracted by the wave-induced stresses, and leads to a more effective downstream transport mechanism. For this case, the cloud acts almost as an isolated blob that propagates downstream.

4.3 Average concentrations

A quantitative way of describing the difference in the particle transport is seen in figures 4.6 and 4.7, for tracer particles ($d_p = 10^{-5}$) and the larger sized particles ($d_p = 10^{-3}$), respectively. In these plots, the point cloud data has been gathered into bins in the streamwise direction. For each bin we have computed the median concentration by the Voronoi method. In order to capture air concentrations only, that deposited particles have been excluded from the statistics. The vertical panels show different times, and by construction, all cases have unity concentration at $t = 0$. Note that even though different puffs have different starting positions, we have shifted the plume centres to $(x, z) = (0, 0)$ for analysis and visualisation purposes.

For the tracer particles in figure 4.6, the flat case appears to have a shorter arrival time than the two wave cases, as seen by the high concentration far downstream at $t = 0.5$. This tendency is weakened as time progresses, but the wind sea case appears to distribute the particles over a wider area in the downstream direction than the two others. Also, the peak concentration location for this
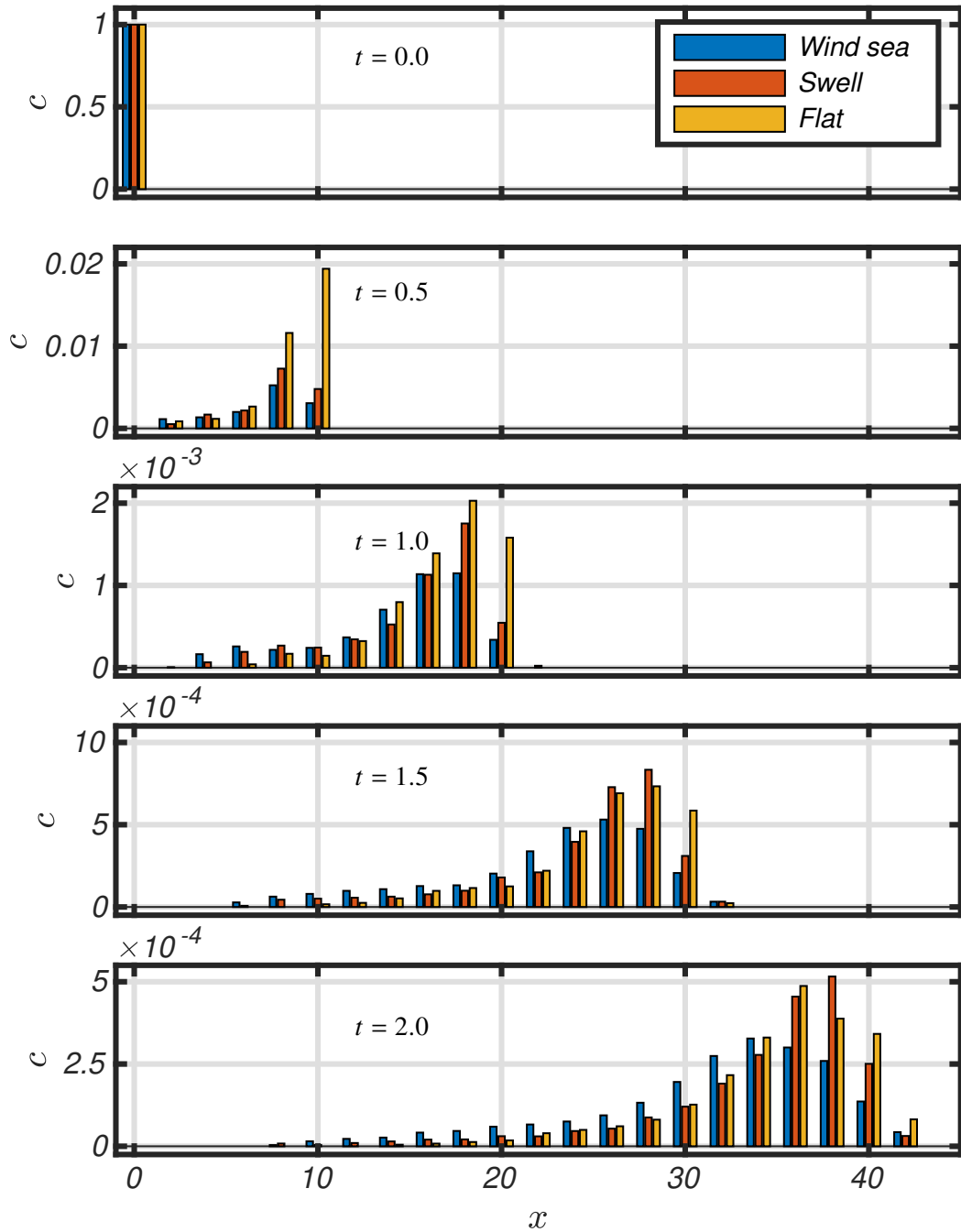
Figure 4.6   Median concentration at downstream locations at different times as computed by the Voronoi method for the three cases and particle size $d_{\mathrm{p}} = 10^{-5}$.
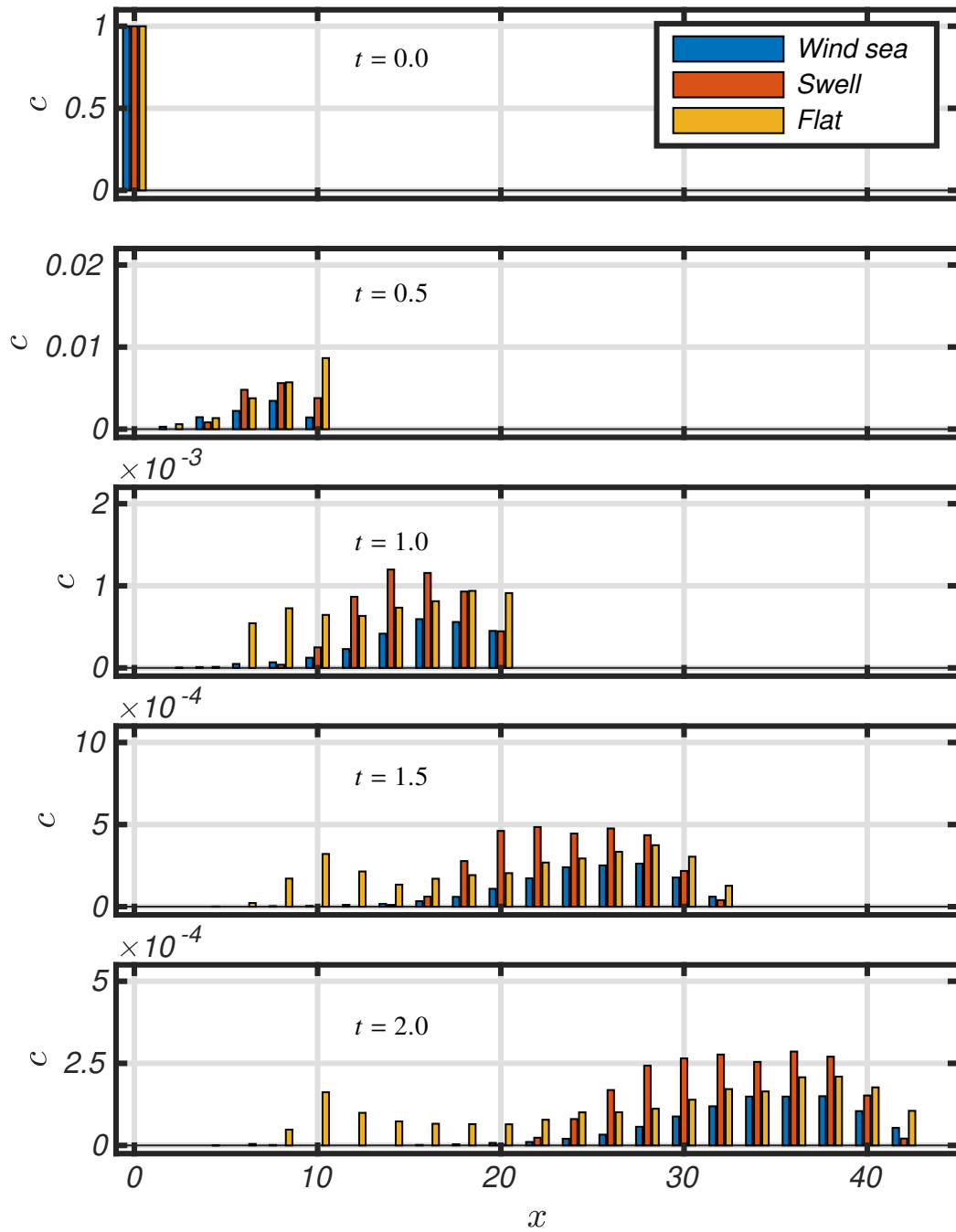
Figure 4.7 Median concentration at downstream locations at different times as computed by the Voronoi method for the three cases and particle size $d_p = 10^{-3}$. For this particle size, deposition for the wind sea case leads to lower concentration downstream.
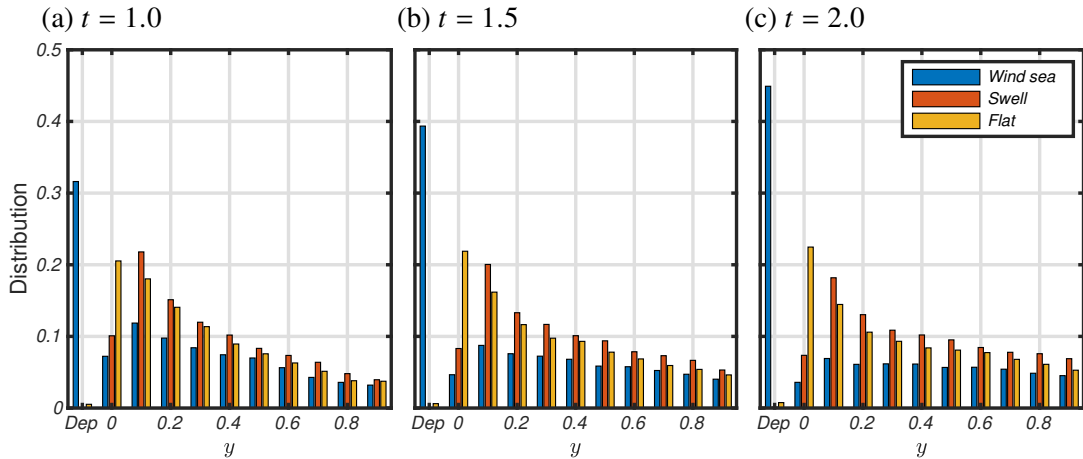
Figure 4.8   *Vertical distribution of particles at $d_{\mathrm{p}} = 10^{-3}$ for wind sea (blue), swell sea (red) and flat (yellow) at time $t = 1.0$ (a), $t = 1.5$ (b) and $t = 2.0$ (c). For the wind sea case there is a considerable amount of deposition occurring.*

case is located further upstream than the two others. This is possibly due to trapping of particles in the cat's eyes.

Figure 4.7 shows the downstream evolution of concentration for the larger particles ($d_{\mathrm{p}} = 10^{-3}$), where, contrary to the tracer particle case, deposition is part of the dynamics. Here, there are relatively large concentration differences between the flat and wave cases at time $t = 0.5$. As time increases, it is clear that the highest concentration is observed for the swell case. For this particle size, the flat case leaves a large number of (un-deposited) particles close to the surface, resulting in a wide extent of the plume in the streamwise direction and a lower concentration far downstream. The wind sea case also leaves particles far upstream (as seen in figure 4.5). However, these are deposited particles that do not contribute to air concentration. It appears that for the wind sea case, deposition is an effective mechanism to reduce the air concentration. The significance of this effect is seen in figure 4.8, which shows the vertical distribution of particles at times $t = \{1.0, 1.5, 2.0\}$. For the wind sea case, more than 30% of the particles have deposited at $t = 1.0$ and almost 45% have deposited at $t = 2.0$. This is a large deposition rate, and in the next section the particle size dependence of the deposition rates is explored in more detail. Another interesting observation that can be made from figure 4.8, is that while the flat case has the largest number of particles located close to the surface, the peak location for the swell case has moved outwards. This may be linked to the outward transport mechanism from the wave-induced stresses.

To sum up, the main differences are: In the wind sea case there is a significant degree of deposition occurring. For the swell case there is an outwards (away from the surface) transport mechanism which counteracts the near surface clustering of particles occurring in the flat case.

4.4   Plume shapes

Many applications rely on plume edge detection. As an example, this is a key ingredient in both Gaussian plume models and in the computational fluid dynamics model based (CFD) CT-Analyst (Boris *et al.*, 2004) approach. To give preliminary input for such modelling, we show the horisontal (figure 4.9 (a,b)) and vertical plume shapes (figure 4.9 (c,d)) of the three cases for two particle sizes. We use the previously defined percentiles to estimate the plume edges, where the crosstream

z-locations in figure 4.9(a,b) are taken as the plus/minus the average of the 10 and 90 percentile in the crosstream direction. For the vertical plume shape in figure 4.9(c,d) we show the 10-, 50-, and 90-percentile (from bottom to top). Also seen are vertical lines signifying the arrival time for the wind sea case. Note that both for the smaller particles ($d_\mathrm{p} = 10^{-5}$) in (a,c) and for the larger particles in ($d_\mathrm{p} = 10^{-3}$), the three cases have similar arrival times. Therefore, only the arrival time for the wind sea is displayed. The arrival time is defined as the 90-percentile *x*-location.

As seen in figure 4.9(a,b), the wind sea case has a slightly wider plume than the two others, regardless of particle size. This may be linked to the increased lateral turbulent transport, as seen in figure 4.1(b), thus supporting the view of wind seas as a rough surface.

For the smaller sized particles, relevant to neutrally buoyant releases of gases, also the vertical shapes are similar, at least beyond $t = 1$, as seen in figure 4.9(c). The main difference here is the slightly higher vertical plume center for the swell sea case. These observations, together with particle plots in figure 4.4 and the concentration plot in figure 4.6, suggest that the traditional Gaussian models may be suitable to describe the transport of light particles (equivalent to neutral gas releases), for turbulent wind over waves.

Interestingly, for the larger particles in figure 4.9 (d), the vertical plume shape for the wind sea is clearly higher than the two others. This is a result of the significant degree of deposition at the surface, and the figure shows only the remaining particles that are still suspended in air. Therefore, the net effect of the increased downward transport introduced by the wind waves, is to deposit a large fraction of the particles on the surface, thus reducing the air concentration significantly (see figure 4.7). The remaining particles end up occupying a region further from the surface than for the two other cases. It is important to note that also the swell sea case has a clear upward shift of the plume compared to the flat case. This is a direct effect of the upward transport mechanism introduced by the swell waves. In terms of streamwise extent of the plume, we recall that figure 4.5 shows that the plumes are much narrower in the streamwise direction than the flat case. These differences in plume shapes and concentrations are expected to give rise to serious issues when attempting to model the contaminant transport for larger sized particles (or non-neutral gas releases) by means of traditional Gaussian models. More specifically, the altered vertical transport appears to yield significant differences in the vertical and horisontal shapes of the plumes.

It is important to realize that the current results are obtained at a laboratory scale. It would therefore be interesting to see future research devoted to reproducing these results on an atmospheric scale.

4.5   Low wave-age deposition - particle size dependence

In the previous section, it could be seen that for the wind sea case, deposition was frequent for the larger sized particles, whereas deposition did not occur for the smaller sized particles. Here, we examine how the deposition rate depends on the particle size, or rather how it depends on the previously defined particle time scale compared to the flow time scale. Figure 4.10 shows the deposition rate for particle sizes

$$d_\mathrm{p} = \{10^{-5}, 3 \cdot 10^{-4}, 6 \cdot 10^{-4}, 8 \cdot 10^{-4}, 10^{-3}, 1.2 \cdot 10^{-3}\}, \tag{4.4}$$

with the corresponding particle (Stokes) time scale

$$\tau_p = \rho_p d_\mathrm{p}^2 \mathrm{Re}/18 = \{9 \cdot 10^{-7}, 7 \cdot 10^{-4}, 3 \cdot 10^{-3}, 6 \cdot 10^{-3}, 9 \cdot 10^{-3}, 12 \cdot 10^{-3}\}. \tag{4.5}$$
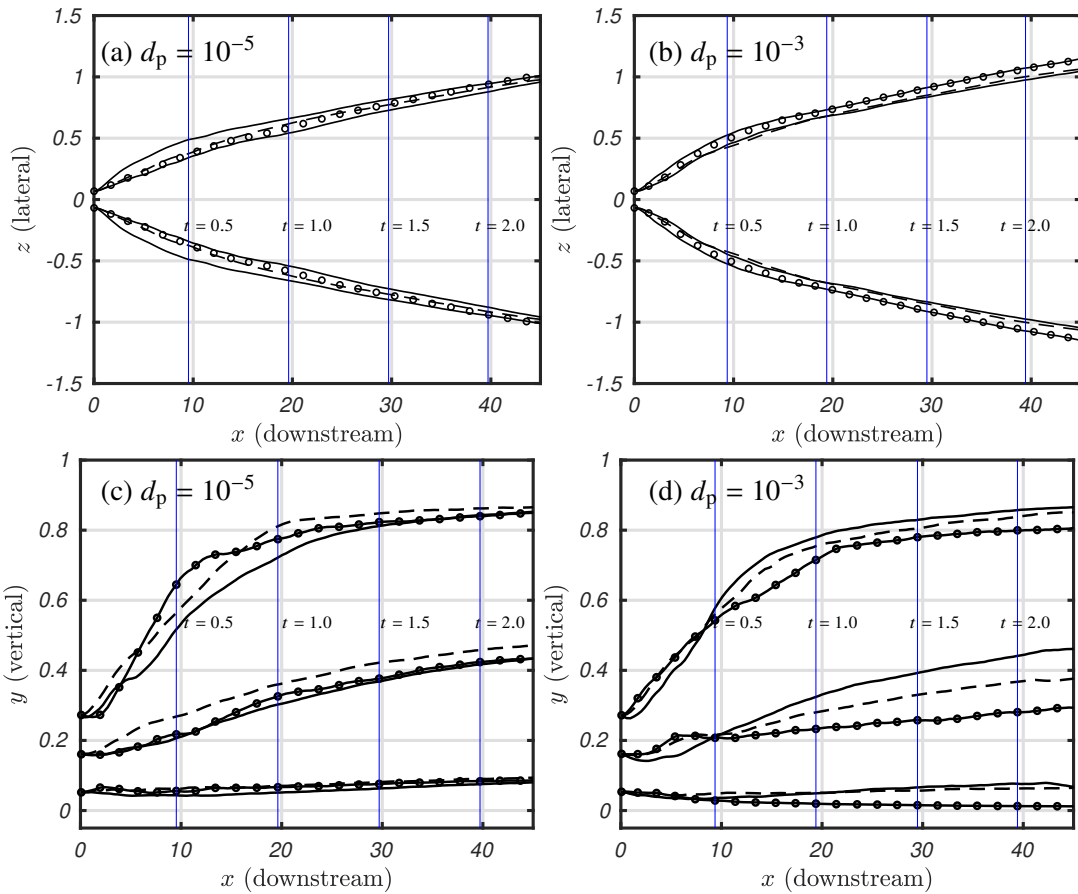
Figure 4.9 *(a and b): Horisontal plume edges for the wind sea case (—), the swell case (--) and the flat case (-•-) as defined by the 90-percentile in the streamwise direction and the 10- and 90-percentile in the crosstream direction. (c and d): Vertical plume shape at different downstream locations (and times) for the wind sea case (—), the swell case (--) and the flat case (-•-) as defined by the 10-, 50-, and 90-percentile in the vertical direction and the 90-percentile in the streamwise direction. The blue vertical lines show the arrival time for the wind sea case.*
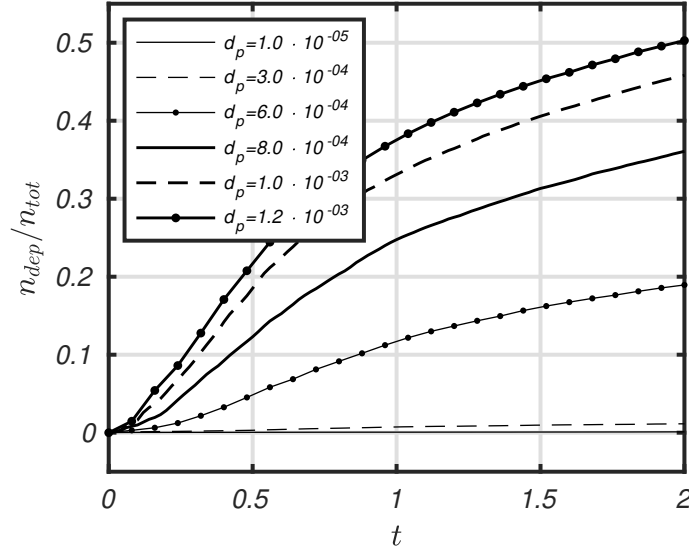
Figure 4.10   Fraction deposited particles versus time for different particle sizes. The particle size are $d_\mathrm{p} = 10^{-5}$ (—), $d_\mathrm{p} = 3 \cdot 10^{-4}$ (--), $d_\mathrm{p} = 6 \cdot 10^{-4}$ (-•-), $d_\mathrm{p} = 8 \cdot 10^{-4}$ (—), $d_\mathrm{p} = 10^{-3}$ (--) and $d_\mathrm{p} = 1.2 \cdot 10^{-3}$ (-•-). Clearly, for the two smallest particle sizes there is almost no deposition. As the particle size increases, so does the deposition rate.

Earlier it was stipulated that a reasonable time scale for the low wave-age case close to the surface is $\tau_F \approx 5 \cdot 10^{-3}$. Given this flow time scale, one would expect that the two smallest particle sizes have small Stokes numbers (since $\tau_p < \tau_F$), and thus should not experience significant deposition. On the other hand, all the larger sized particles will have unity or higher Stokes numbers close to the surface. The figure indeed shows that the deposition rate is small for the two smallest particle sizes. As the particle size increases, so does the deposition rate. However, we note that there is a larger increase in deposition rate from $d_\mathrm{p} = 6 \cdot 10^{-4}$ to $d_\mathrm{p} = 8 \cdot 10^{-4}$ than from $d_\mathrm{p} = 8 \cdot 10^{-4}$ to $d_\mathrm{p} = 10^{-3}$.

We have not explored the upper limit of particle size, but particle sizes of the order $d_\mathrm{p} > 1.5 \cdot 10^{-3}$ are too large and slow to respond in any reasonable manner to flow changes. Note that this is an inherent weakness in using a low Reynolds number flow. A low Reynolds number implies a small separation between large and small length scales in the flow (Pope, 2000), and therefore adds an (unrealistically low) upper limit to the particle size that can be studied.

4.6   Deposition mechanism

So far we have concluded that large particles are prone to deposition in the wind sea regime, whereas the same particles tend to leave the surface area for the swell case. Figure 4.11 shows an example of a particle path for the swell case and a relatively small particle size ($d_\mathrm{p} = 3 \cdot 10^{-4}$). Note that in the figure, the colour of the curve is the local Stokes number experienced by the particle

$$\mathrm{St} = \frac{\tau_p}{\tau_s}, \tag{4.6}$$

where τ_S (defined in equation (2.33)) is the inverse strain-rate magnitude of the flow. Close to the surface ($y < 0.1$), this definition of the Stokes number is expected to give a good estimate as
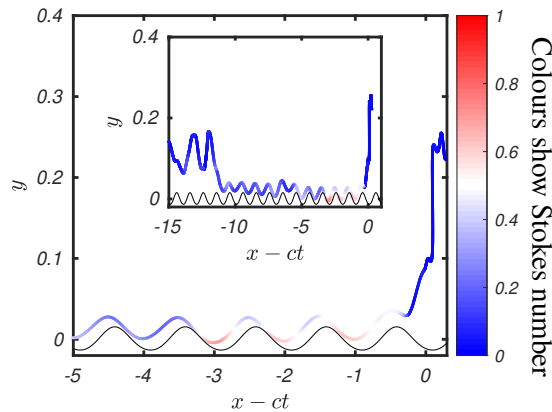
Figure 4.11   Particle path in the frame of reference that moves with the swell wave ($c_* = 19.9$). Example of escape from the surface for the swell case and particle size $d_\mathrm{p} = 3 \cdot 10^{-4}$.

to whether or not particles are able to follow the flow. However, in the outer part of the domain, this may not be the correct Stokes number (since mean flow transport would have a smaller time scale than the time scale given by the strain rate). In the figure, we use a frame of reference that follows the propagating wave. Hence, in that frame, the wave shape is stationary. From the colors on the path line, we clearly observe that the time scale of the flow is small close to the surface (because the Stokes number is close to unity), and especially in the wave through. This behaviour is in line with the one phase results shown in figure 4.3. As the particle enters the surface region it experiences large gradients in the flow, and is unable to follow the streamline. Upstream (in the frame of reference that moves with the wave) of the crest the wave-induced stresses result in a downward transport mechanism. However, since the particle is reluctant to respond to this downward transport, it is transported with the mean flow to the next crest. Here, the wave-induced stresses excert an upward force. The particle also has trouble keeping up with this motion, and the end result throughout a cycle (or a wave length) is that the particle is transported somewhat outwards. Therefore, slowly the particle is able to leave the surface area and re-enter the outer part of the flow. Similar tendencies is seen for a large number of particles, and also for the other particle sizes.

Figure 4.12 show two particle paths for the wind sea case and $d_\mathrm{p} = 3 \cdot 10^{-4}$. Unlike the swell case, here the phase speed of the wave is small and the particle will move from left to right in most of the domain. In figure 4.12 (a), the particle path for a non-depositing particle is shown. The particle enters the critical layer approximately in the center between two crests, and is not drawn down towards the surface. Instead, the particle behaves more or less as we would expect from a passive fluid particle, circulating around the critical layer. Thus, apparently, particles entering the surface layer between two crests never experience high lokal Stokes numbers. On the other hand, in figure 4.12 (b), we see a particle that enters the critical layer on the upwind side of the crest. Here, as seen in figure 4.3, the time scale of the flow is small, thus resulting in a large local Stokes number. Clearly, the particle is unable to follow the streamlines of the flow, and consequently it is deposited on the surface.

These results were shown for relatively small particles. As the particle size increases so will the region in which large Stokes numbers are experienced. Since the critical layer introduces orbital
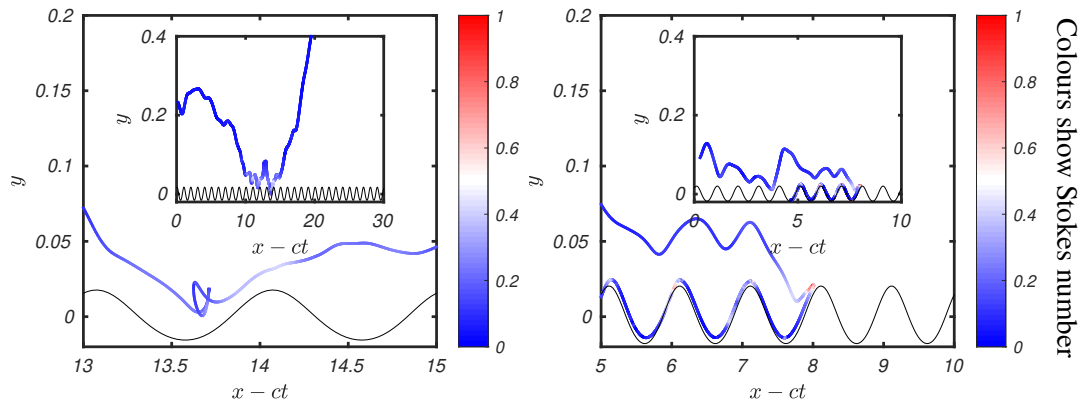
Figure 4.12 *Particle path in the frame of reference that moves with the wind wave ($c_* = 2.8$).*
Example of (a) cat's eyes trapping and (b) deposition for particle size $d_\mathrm{p} = 3{\cdot}10^{-4}$.

motion, the end result is increased deposition with increased particle size. The upper bound on this process is expected to be based on whether particles are able to respond to the turbulent eddies that shed particles down into this region. In this report, we have excluded the effect of gravitational settling. On a larger scale, this effect needs to be accounted for. If this effect is taken into account, one also has to include the time scale given by the settling velocity in the analysis.

5   Conclusions

This report deals with aerosol transport in turbulent airflow over a free water surface. For this flow, three important regimes that need to be explored are: In the first one, the wind is not capable of creating waves; and the sea surface is flat. The second regime is when the winds are sufficently strong to generate water waves. These so called wind waves have relatively small wave lengths and slow propagation speeds. The bulk effect of these waves is that the surface provides aerodynamic drag. The third regime occurs when distantly generated waves propagate into regions of calmer winds. These so called swell waves have long wave lengths and fast propagation speeds.

In this report we compare aerosol transport for these three regimes by means of computational fluid dynamics (CFD). Generally, the interaction of wind and waves depend on a number of parameters, such as the ratio of the wind to the wave speed, the angle between the wind and the waves and the wave steepness. To map out this parameter space is virtually impossible given the high computational cost of one CFD simulation. Therefore, based on previous experience, we chose one representative case for each of the two wave cases. In order to capture the effect of deposition on the water surface we solved the turbulent motion in the air as well as the wave propagation in the water, and a particle method is used to track a large number of particles.

In line with existing litterature we find that the wind sea behaves as a rough surface. For the dispersion of aerosols, this has two major consequences. Firstly, crosstream transport is enhanced, which leads to a slightly wider plume. Secondly, and arguably most important, there is a downward transport mechanism present, which leads to deposition of particles at the surface if the particles are sufficiently large. Our results show that this is linked to the so called Kelvin cat's-eyes, where particles are trapped in recirculation regions close to the surface. Clustering of particles close to the surface is also seen for the flat case, but deposition on the surface is not frequent. As a consequence, for wind seas there is reduced air concentrations compared to the flat case.

In the swell wave regime, the plume width and the plume arrival time is similar to the flat surface regime. However, since the waves are feeding momentum to the air, there is an upward transport mechanism. The most important consequence of this, is that the near surface clustering of larger particles, present in the flat surface case, is counteracted. This leads to higher concentrations downstream of the source.

The similarity in plume shape and arrival time between the flat case, the wind sea case, and the swell sea case for small particles suggests that the simplified operational dispersion models, such as Gaussian models, may be used for transport of neutral gases over waves. However, the results point to some differences in the concentration distribution between the three cases.

For larger particles this report shows clear evidence of altered dynamics both for wind seas and swell seas compared to the flat boundary layer flow. These effects are currently not captured by simplified dispersion models, but may prove to be important.

The current results are obtained at a laboratory scale, and further research is warranted to investigate the effects on relevant atmospheric scales.

References

ÅKERVIK, E. & VARTDAL, M. 2016 Simulation of Two-Phase Interface Flows. *Tech. Rep.* 00822. FFI, Norwegian Defence Research Establishment.

ARYA, S. P. S. 1975 A drag partition theory for determining the large-scale roughness parameter and wind stress on the arctic pack ice. *J. Geophys. Res.* **80** (24), 3447–3454.

ASHGRIZ, N. & POO, J. Y. 1991 FLAIR: Flux Line-Segment Model For Advection and Interface Reconstruction. *J. Comp. Phys.* **93** (2), 449–468.

BARBER, C. B., DOBKIN, D. P., & HUHDANPAA, H. 1996 The quickhull algorithm for convex hulls. *ACM Trans. Math. Softw. (TOMS)* **22** (4), 469–483.

BELAMARI, S. 2005 Report on uncertainty estimates of an optimal bulk formulation for surface turbulent fluxes. *Marine Envir. Sec. Europe (MERSEA IP), Del. D* **4**.

BELCHER, S. E. & HUNT, J. C. R. 1993 Turbulent shear flow over slowly moving waves. *J. Fluid Mech.* **251**, 109–148.

BELCHER, S. E. & HUNT, J. C. R. 1998 Turbulent flows over hills and waves. *Annu. Rev. Fluid Mech.* **30**, 507–38.

BORIS, JAY, FULTON JR, JACK E, OBENSCHAIN, KEITH, PATNAIK, GOPAL & YOUNG JR, THEODORE 2004 Ct-analyst: fast and accurate cbr emergency assessment. In *Chemical and Biological Sensing V*, , vol. 5416, pp. 1–13. International Society for Optics and Photonics.

CHARNOCK, H 1955 Wind stress on a water surface. *Quart. J. Royal Met. Soc.* **81** (350), 639–640.

COHEN, J. E. & BELCHER, S. E. 1999 Turbulent shear flow over fast-moving waves. *J. Fluid Mech.* **386**, 345–371.

DEIKE, L., MELVILLE, W. K. & POPINET, S. 2016 Air entrainment and bubble statistics in breaking waves. *J. Fluid Mech.* **801**, 91–129.

DESKOS, GEORGIOS, LEE, JOSEPH, DRAXL, CAROLINE & SPRAGUE, MICHAEL 2021 Review of wind–wave coupling models for large-eddy simulation of the marine atmospheric boundary layer. *Journal of the Atmospheric Sciences* .

DONELAN, M. A. 1998 Air-water exchange processes. *Coastal and Estuarine Studies* pp. 19–36.

EDSON, J., CRAWFORD, T., CRESCENTI, J., FARRAR, T., FREW, N., GERBI, G., HELMIS, C., HRISTOV, T., KHELIF, D., JESSUP, A. & OTHERS 2007 The coupled boundary layers and air–sea transfer experiment in low winds. *Bul. Am. Met. Soc.* **88** (3), 341–356.

FAIRALL, CW, BRADLEY, EDWARD F, HARE, JE, GRACHEV, AA & EDSON, JB 2003 Bulk parameterization of air–sea fluxes: Updates and verification for the coare algorithm. *J. Climate* **16** (4), 571–591.

HAM, F., MATTSSON, K. & IACCARINO, G. 2006 Accurate and stable finite volume operators for unstructured flow solvers. *Tech. Rep.*. Center For Turbulence Research (CTR).

HAM, F., MATTSSON, K., IACCARINO, G. & MOIN, P. 2007 Towards time-stable and accurate LES on unstructured grids. *Comp. Effects in LES* pp. 235–249.

HANNA, STEVEN R, BRIGGS, GARY A & HOSKER JR, RAYFORD P 1982 Handbook on atmospheric diffusion. *Tech. Rep.*. National Oceanic and Atmospheric Administration, Oak Ridge, TN (USA . . . .

HASSELMANN, K., BARNETT, T. P., BOUWS, E., CARLSON, H., CARTWRIGHT, D. E., ENKE, K., EWING, J. A., GIENAPP, H., HASSELMANN, D. E., KRUSEMAN, P. & OTHERS 1973 Measurements of wind-wave growth and swell decay during the joint north sea wave project (jonswap). *Ergänzungsheft 8-12* .

JANSSEN, P. A. E. M., DOYLE, J. D., BIDLOT, J., HANSEN, B., ISAKSEN, L. & VITERBO, P. 2002 Impact and feedback of ocean waves on the atmosphere. *Adv. Fluid Mech.* **33**, 155–198.

JEFFREYS, H. 1925 On the formation of water waves by wind. *Proceedings of the Royal Society of London. Series A, Containing Papers of a Mathematical and Physical Character* **107** (742), 189–206.

KAHMA, K. K., DONELAN, M. A., DRENNAN, W. M. & TERRAY, E. A. 2016 Evidence of energy and momentum flux from swell to wind. *J. Phys. Oceanogr.* **46** (7), 2143–2156.

KIM, D., MAIN, A. & MOIN, P. 2014 Investigation of bubble formation by breaking waves in turbulent two-phase couettte flow. In *30th Symp. Naval Hydr., Hobart, Tasmania, Australia, 2-7 Nov. 2014*.

KUDRYAVTSEV, V. N., MAKIN, V. K. & MEIRINK, J. F. 2001 Simplified model of the air flow above waves. *Bound. Lay. Met.* **100**, 63–90.

KUNDU, P. K., COHEN, I. M. & DOWLING, D. R. 2012 *Fluid Mechanics*, 5th edn. Elsevier Academic Press.

LAMB, H. 1932 *Hydrodynamics*. Cambridge University Press.

MAHESH, K., CONSTANTINESCU, G. & MOIN, P. 2004 A numerical method for large-eddy simulation in complex geometries. *J. Comp. Phys.* **197**, 215–240.

MASTENBROEK, C., MAKIN, V. K., GARAT, M. H. & GIOVANANGELI, J.-P. 1996 Experimental evidence of the rapid distortion of turbulence in the air flow over water waves. *J. Fluid Mech.* **318**, 273–302.

MILES, J. W. 1957 On the generation of surface waves by shear flows. *J. Fluid Mech.* **3**, 185–204.

MORTAZAVI, M., LE CHENADEC, V., MOIN, P. & MANI, A. 2016 Direct numerical simulation of a turbulent hydraulic jump: turbulence statistics and air entrainment. *J. Fluid Mech.* **797**, 60–94.

PARKER, B. J. & YOUNGS, D. L. 1992 *Two and Three Dimensional Eulerian Simulation of Fluid Flow With Material Interfaces*. Atomic Weapons Establishment.

POPE, S. B. 2000 *Turbulent flows*. Cambridge university press.

Sardina, G., Schlatter, P., Brandt, L., Picano, F. & Casciola, C. M. 2012 Wall accumulation and spatial localization in particle-laden wall flows. *J. Fluid Mech.* **699**, 50–78.

Schwarzkopf, J. D., Sommerfeld, M., Crowe, C. T. & Tsuji, Y. 2012 *Multiphase flows with droplets and particles*. Boca Raton, Florida, U.S.: CRC press, Taylor & Francis Group.

Smits, A. J., McKeon, B. J. & Marusic, I. 2011 High-reynolds number wall turbulence. *Annu. Rev. Fluid Mech.* **43**, 353–375.

Stull, Roland B 1988 *An introduction to boundary layer meteorology*, , vol. 13. Springer Science & Business Media.

Sullivan, P. P., Edson, J. B., T., Hristov & McWilliams, J. C. 2008 Large-eddy simulations and observations of atmospheric marine boundary layers above nonequillibrium surface waves. *J. Atmos. Sci.* **65**, 1225–1245.

Sullivan, P. P., McWilliams, J. C. & Moeng, C-H. 2000 Simulation of turbulent flow over idealized waves. *J. Fluid Mech.* **404**, 47–85.

Yang, D. & Shen, L. 2009 Characteristics of coherent vortical structures in turbulent flows over progressive waves. *Phys. Fluids* **21**, 125106.

Yang, D. & Shen, L. 2010 Direct-simulation-based study of turbulent flow over various waving boundaries. *J. Fluid Mech.* **650**, 131–180.

Yang, D. & Shen, L. 2017 Direct numerical simulation of scalar transport in turbulent flows over progressive surface waves. *J. Fluid Mech.* **819**, 58–103.

Åkervik, E. & Vartdal, M. 2019 The role of wave kinematics in turbulent flow over waves. *J. Fluid Mech.* **880**, 890–915.

About FFI
The Norwegian Defence Research Establishment (FFI) was founded 11th of April 1946. It is organised as an administrative agency subordinate to the Ministry of Defence.
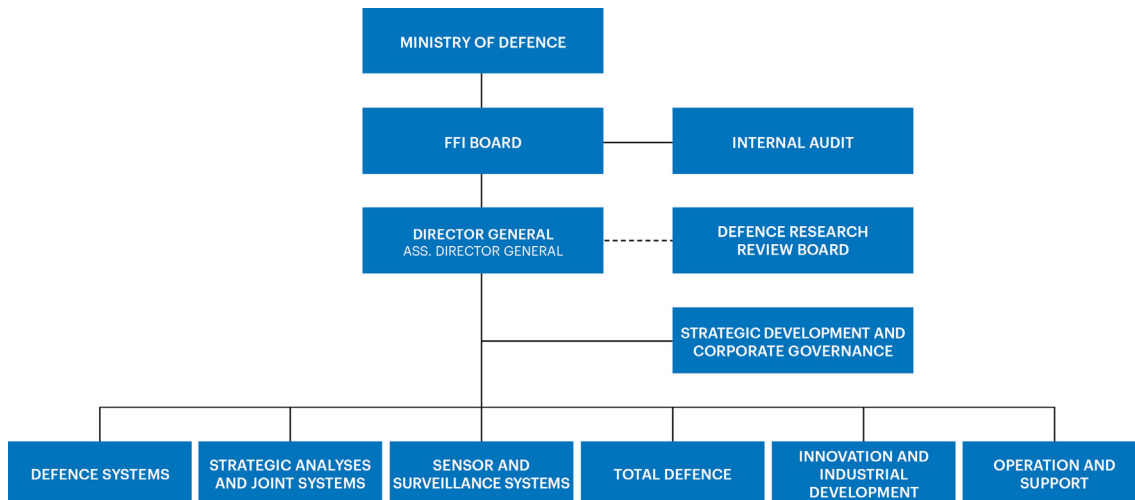
FFI's mission
FFI is the prime institution responsible for defence related research in Norway. Its principal mission is to carry out research and development to meet the requirements of the Armed Forces. FFI has the role of chief adviser to the political and military leadership. In particular, the institute shall focus on aspects of the development in science and technology that can influence our security policy or defence planning.

FFI's vision
FFI turns knowledge and ideas into an efficient defence.

FFI's characteristics
Creative, daring, broad-minded and responsible.